

Spatial zonation limits magnesite dissolution in porous media

Li Li^{a,c,*}, Fatemeh Salehikhoo^a, Susan L. Brantley^{b,c}, Peyman Heidari^a

^a John and Willie Leone Department of Energy and Mineral Engineering, The Pennsylvania State University, University Park, PA 16802, United States

^b Department of Geosciences, The Pennsylvania State University, University Park, PA 16802, United States

^c Earth and Environmental Systems Institute, The Pennsylvania State University, University Park, PA 16802, United States

Received 24 April 2013; accepted in revised form 30 October 2013; available online 12 November 2013

Abstract

We investigate how mineral spatial distribution in porous media affects their dissolution rates. Specifically, we measure the dissolution rate of magnesite interspersed in different patterns in packed columns of quartz sand where the magnesite concentration (v/v) was held constant. The largest difference was observed between a “Mixed column” containing uniformly distributed magnesite and a “One-zone column” containing magnesite packed into one cylindrical center zone aligned parallel to the main flow of acidic inlet fluid (flow-parallel One-zone column). The columns were flushed with acid water at a pH of 4.0 at flow velocities of 3.6 or 0.36 m/d. Breakthrough data show that the rate of magnesite dissolution is 1.6–2 times slower in the One-zone column compared to the Mixed column. This extent of rate limitation is much larger than what was observed in our previous work (14%) for a similar One-zone column where the magnesite was packed in a layer aligned perpendicular to flow (flow-transverse One-zone column). Two-dimensional reactive transport modeling with CrunchFlow revealed that ion activity product (IAP) and local dissolution rates at the grid block scale (0.1 cm) vary by orders of magnitude. Much of the central magnesite zone in the One-zone flow-parallel column is characterized by close or equal to equilibrium conditions with $IAP/K_{eq} > 0.1$. Two important surface areas are defined to understand the observed rates: the effective surface area (A_e) reflects the magnesite that effectively dissolves under far from equilibrium conditions ($IAP/K_{eq} < 0.1$), while the interface surface area (A_I) reflects the effective magnesite surface that lies along the quartz–magnesite interface. Modeling results reveal that the transverse dispersivity at the interface of the quartz and magnesite zones controls mass transport and therefore the values of A_e and A_I . Under the conditions examined in this work, the value of A_e varies from 2% to 67% of the total magnesite BET surface area. Column-scale bulk rates $R_{MgCO_3,B}$ (in units of mol/s) vary linearly with A_e and A_I . Using A_e to normalize rates, we calculate a rate constant ($10^{-9.56}$ mol/m²/s) that is very close to the value of $10^{-10.0}$ mol/m²/s under well-mixed conditions at the grid block scale. This implies that the laboratory-field rate discrepancy can potentially be caused by differences in the effective surface area. If we know the effective surface area of dissolution, we will be able to use the rate constant measured in laboratory systems to calculate field rates for some systems. In this work, approximately 60–70% of the A_e is at the magnesite–quartz interface. This implies that in some field systems where the detailed information that we have for our columns is not available, the effective mineral surface area may be approximated by the area of grains residing at the interface of reactive mineral zones. Although it has long been known that spatial heterogeneities play a significant role in determining physical processes such as flow and solute transport, our data are the first that systematically and experimentally quantifies the importance of mineral spatial distribution (chemical heterogeneity) on dissolution.

© 2013 Elsevier Ltd. All rights reserved.

1. INTRODUCTION

* Corresponding author at: John and Willie Leone Department of Energy and Mineral Engineering, Pennsylvania State University, University Park, PA 16802, United States. Tel.: +1 814 867 3547.
E-mail address: lili@eme.psu.edu (L. Li).

Mineral reactions play an important role in applications relevant to water, energy, and environment. These reactions affect the chemistry of surface and groundwater

(Hamzaoui-Azaza et al., 2011; Zhu and Schwartz, 2011), change reservoir structural properties during energy production (Pruess, 2008; Taron and Elsworth, 2009), affect the transport and fate of contaminants (Liu et al., 2004; Frye et al., 2012; Iwakun et al., 2012), and influence global elemental cycles and climate change (Godderis et al., 2013, 2010). Mineral reaction kinetics have been studied extensively in well-mixed laboratory systems, in homogeneously packed columns (Van Grinsven and Van Riemsdijk, 1992; Taylor et al., 2000), and in the natural subsurface using field weathering profiles (Anbeek, 1993; Casey et al., 1993; White, 2002; Maher et al., 2004; Brantley and White, 2009). Significant progress has been made in understanding rates under an array of geological and climate conditions (Jeschke and Dreybrodt, 2002; Brantley, 2010; Banwart et al., 2011; Chorover et al., 2011; Lin et al., 2011). For more than three decades, however, rates measured in the subsurface have been reported to be 3–5 orders of magnitude lower than those measured under laboratory conditions (Casey, 1987; Casey et al., 1993; Velbel, 1993; Anderson et al., 2002; White and Brantley, 2003; Navarre-Sitchler and Brantley, 2007; Brantley and White, 2009). A variety of factors have been proposed to explain this long-standing rate discrepancy, including, for example, the effects of reaction affinity, the age of reactive minerals, secondary mineral precipitation, dynamic porosity evolution, and residence time (Anbeek, 1993; White and Brantley, 1995; Alekseyev et al., 1997; Zhu, 2005; Maher et al., 2006; Maher, 2010; Zhu et al., 2010).

In the subsurface, spatial heterogeneity, defined here as the non-uniform spatial distribution of mineral concentration within geomedial, is the norm rather than exception. Mineral phases occur in nature with various spatial patterns at different spatial scales. Distributions vary from random and uniform patterns at one extreme, to clustered or layered patterns at the other end of the spectrum (Scheibe et al., 2006; Liu et al., 2008; Landrot et al., 2012; Peng et al., 2012). This leads to significant spatial variations in mineralogical, geochemical, and physical properties (Gelhar, 1993; Scheibe et al., 2006; Jin et al., 2010; Taylor and Macquaker, 2011). In hydrogeology, physical heterogeneity has been known to control flow and solute transport processes for more than three decades (Gelhar and Axness, 1983; Berkowitz and Scher, 2001; Sudicky et al., 2010; Castro-Alcala et al., 2012). Likewise, the effects of such heterogeneities are well known in environmental engineering. For example, the distribution of spilled oil residues has been found to determine the time scale of remediation and biodegradation (Brusseau et al., 2000; Yoon et al., 2008, 2009; Zhang et al., 2008; DiFilippo et al., 2010). Most studies, however, have focused on spatial variations in physical properties, including porosity, permeability, and flow paths.

Compared to decades of literature on the effects of spatial heterogeneity on physical processes, studies on the effects of mineral distribution on (bio)geochemical processes are scarce even though they have been acknowledged for decades (Knapp, 1989). Mineral reactions typically involve multiple chemical species that are coupled through non-linear reaction thermodynamics and kinetics. A few experimental and modeling studies have shown that

the structure of the porous medium controls reaction rates (Li et al., 2006, 2007a; Liu et al., 2008, 2013; Tartakovsky et al., 2008; Rolle et al., 2009; Hochstetler et al., 2013). For example, rates of calcite precipitation in microfluidic and Darcy-scale experiments have been found to be limited by transverse mixing between the Ca(II)-containing and carbonate-containing waters, which strongly depends on the structure of porous media (Willingham et al., 2008; Zhang et al., 2010; Yoon et al., 2012). Field experiments have documented the controls of both physical and geochemical heterogeneities on biogeochemical reaction rates during biostimulation (Scheibe et al., 2006; Li et al., 2010; Yabusaki et al., 2011). Fractured rocks naturally represent heterogeneous systems with significant contrast between the fracture and matrix. Reactions between fractured rocks and fluid have been studied with a main focus on how mineral reactions alter porosity, permeability, surface area, and fracture structure (Detwiler et al., 2003; Gouze et al., 2003; Detwiler, 2010; Noiriél et al., 2010; McGuire et al., 2013). The role of mineral distribution has rarely been explored systematically in ways that allow comparisons among systems with different patterns of mineral distributions.

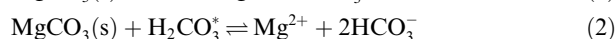
In our previous work (Salehikhoo et al., 2013), columns were set up with two spatial distributions. One pattern was referred to as “Mixed”: a column with an 11% (v/v) concentration of magnesite randomly and uniformly distributed within a quartz sand matrix. The other pattern was referred to as “One-zone”: a column with 11% (v/v) magnesite distributed in one layer that was oriented perpendicular to the main flow direction. More than fifty flow-through experiments were run to measure magnesite dissolution rates under conditions of variable mineral distribution, column lengths, and flow velocities. At maximum, the magnesite dissolution rate was 14% higher in the Mixed column compared to the One-zone column. The largest difference was observed in moderate flow regimes where the reaction was neither limited by interfacial kinetics nor by transport alone. The column-scale rates were observed to vary with the Damkohler number, defined as the ratio of the time scales of advection relative to that of chemical equilibration. The zoned column experiment published in our previous work is referred to here as “flow-transverse One zone”.

In this new contribution we now explore the magnesite dissolution rates for columns with 11% (v/v) magnesite packed within a quartz sand matrix where the magnesite is packed in zones aligned parallel to the main flow (“flow-parallel One-zone column”). In effect, our columns provide experimental models of dissolution of natural systems where flow is either aligned perpendicular to the main flow direction (Salehikhoo et al., 2013) or parallel to the main flow direction (this work). Magnesite was chosen because carbonates are one of the most abundant minerals in sedimentary rocks (Morse and Arvidson, 2002; Morse et al., 2007) and are important in many applications (Biswas et al., 2011; Krumins et al., 2013). In addition, magnesite dissolution has been studied extensively in well-mixed reactors and is known to dissolve readily (Chou et al., 1989; Saldi et al., 2010). However, its dissolution has not been studied under coupled flow and transport conditions except in our recent study (Salehikhoo et al., 2013). Here

we use four columns with the same concentration of magnesite packed in different patterns, i.e., Mixed, Three-zone, Two-zone, and One-zone columns (Fig. 1A). The column experiments were flushed with acidic solutions at flow velocities of 0.36 and 3.6 m/d. To understand the mechanism explaining the effects of spatial zonation, a two-dimensional reactive transport model was applied to interpret the tracer and Mg breakthrough data.

2. MAGNESITE DISSOLUTION

Magnesite dissolution thermodynamics and kinetics have been documented extensively (Chou et al., 1989; Pokrovsky et al., 2009; Saldi et al., 2009, 2010; Benzeeth et al., 2011; Saldi et al., 2012). As has become the norm in reactive transport models, we use here the rate laws based on solution chemistry rather than mineral surface complexation. Specifically, we model three parallel reaction paths (Plummer and Wigley, 1976; Chou et al., 1989):



The Transition State Theory (TST)-based rate law for these reactions is written as follows:

$$r_{\text{MgCO}_3} = \left(k_1 a_{\text{H}^+} + k_2 a_{\text{H}_2\text{CO}_3^*} + k_3 \right) A \left(1 - \frac{\text{IAP}}{K_{\text{eq}}} \right) \quad (4)$$

Here k_1 , k_2 , and k_3 are the rate constants ($\text{mol m}^{-2} \text{s}^{-1}$) for their corresponding reactions, a_{H^+} and $a_{\text{H}_2\text{CO}_3^*}$ are the activities of hydrogen ion and carbonic acid (dimensionless), A is the mineral surface area (m^2). Typically the Brunauer–Emmett–Teller (BET) area is used for the rate calculation. The ion activity product (IAP) is defined as $a_{\text{Mg}^{2+}} a_{\text{CO}_3^{2-}}$,

and K_{eq} is the equilibrium constant for reaction (3). The saturation index value of IAP/K_{eq} is a measure of the distance from equilibrium – a value of 1.0 denotes equilibrium and values close to zero denote far from equilibrium. The fact that the saturation index values are the same for all three reactions can be easily proved by explicitly writing the IAP/K_{eq} expressions for each reaction pathway. The rate law (Eq. (4)) reveals that magnesite reaction rates depend on its intrinsic reactivity (k_1 , k_2 , k_3), surface area (A), and aqueous geochemistry (IAP). Note that the rates of each of the three reactions dominate different conditions within the overall geochemical reaction space. For example, the rate of the first reaction dominates under acidic conditions where pH is below ~ 5 , the rate of the second reaction dominates when CO_2 concentrations are high, and the last rate dominates when pH is higher than 6–7.

3. METHODOLOGY

3.1. Column experiments

3.1.1. Mineral spatial distribution

We use four columns of 10.5 cm in length and 2.56 cm in diameter. For easy comparison, the mineral properties (including grain size and surface area), the proportion of magnesite versus quartz, the preparation procedures, and flow-through experiments are the same as in our previous study (Salehikhoo et al., 2013). The only difference is the orientation of the magnesite zones relative to the main flow direction. The columns were packed with the same concentration ($11.5 \pm 0.5\%$, v/v) of magnesite within a quartz sand matrix in four patterns: Mixed, Three-zone, Two-zone, and One-zone columns (Fig. 1A). In the Mixed column, magnesite was uniformly distributed. In the One-zone column, magnesite was packed in the middle of the quartz matrix

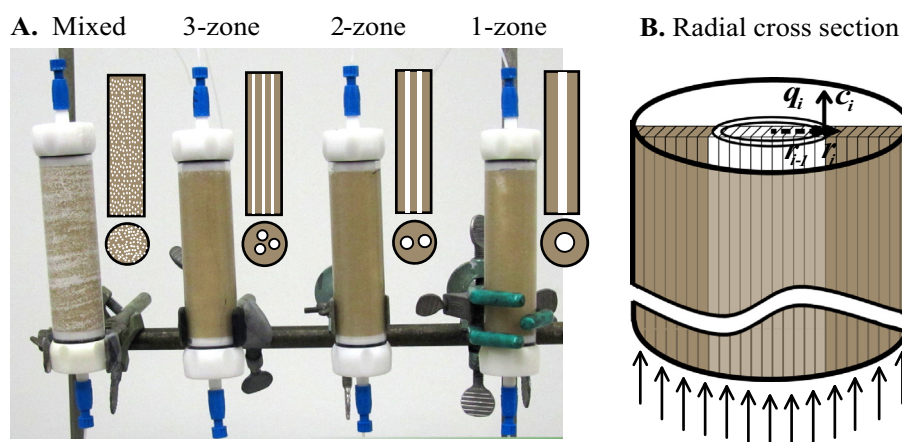


Fig. 1. (A) A photo of the packed columns showing the four different spatial distributions of magnesite (white) and quartz (sand color). Above each column to the right are cross-sections showing either a section cut in parallel to the flow direction (above) or perpendicular to flow direction (below). In all columns, the volume fraction of magnesite in quartz matrix is $11.5\% \pm 0.5\%$ (v/v). The Mixed column consists of a random, uniform mixture of magnesite and quartz. In the other columns, the magnesite grains are aligned in cylindrical zones within a matrix of quartz such that the cylinders are oriented in the direction parallel to the main flow. (B) Radial cross-section representation for the One-zone column. The symbols q_i and c_i represent the flow rates and concentrations out from the annulus between r_{i-1} and r_i . Fluid flowed upward for all columns. (For interpretation of the references to color in this figure legend, the reader is referred to the web version of this article.)

as one cylindrical zone with a diameter of 10.97 mm aligned parallel to the main flow (Fig. 1B). In that center zone, the concentration of magnesite was maintained as close to 100% as possible. In the Three-zone and Two-zone columns, magnesite was distributed as three and two cylindrical zones with diameters of 6.0 and 7.4 mm, respectively. Again, each zone contained as close to 100% magnesite as possible during packing. The properties of each column are shown in Table 1.

3.1.2. Material preparation

The magnesite (from Mongolia) was examined by X-ray diffraction analysis and was found to contain no other detectable crystalline phases. Analysis by Inductively Coupled Plasma Emission Spectrometry (ICP-AES) revealed 28.3 wt% Mg (compared to an expected value of 28.6 wt% based on the stoichiometry of MgCO_3). Magnesite grains were sieved to a size interval of 354–500 μm (sieve numbers 30 and 40). This same size range was used for quartz grains to ensure physical homogeneity of the column. To clean grain surfaces, the magnesite specimen was treated with 1% HCl for several seconds and was ultrasonically cleaned in spectroscopic-grade acetone to remove fine particles following standard practice (Brantley, 2004). The samples were then rinsed with distilled water, dried in an oven at 60 °C, and stored in a desiccator. The surface area was determined by N_2 gas sorption using the Brunauer–Emmett–Teller (BET) method (Micromeritics ASAP-2020 surface analyzer). The average BET surface area of magnesite and quartz sand was measured to be 1.87 ± 0.54 and $0.097 \pm 0.028 \text{ m}^2/\text{g}$, respectively. A similar cleaning procedure was followed for quartz grains from Unimin Corporation except without the HCl treatment.

3.1.3. Column packing procedure

A “wet packing” method (Minyard and Burgos, 2007) was used with the initial solution specified in Table 2. For the Mixed column, magnesite and quartz grains were mixed to generate a homogeneous mixture. The column was packed in 10 increments with 1/10 of the total mass added to the solution in the column in each increment. For the

One-zone column, magnesite and quartz were also packed in 10 increments. However, a thin plastic tube with a diameter of 10.97 mm was vertically placed in the center of the column to align the magnesite grains in place. In each increment, the initial solution was poured slowly into the column to establish a height of approximately 1 cm with one portion of magnesite and quartz added into and outside of the plastic tube, respectively. After each step, the tube was gently pulled out of the matrix to avoid excessive mixing of magnesite and quartz. Columns were tapped on the four sides to remove air bubbles and ensure uniformity. After packing, the columns were secured with the end-cap and connected to a syringe pump (Harvard Apparatus MA1 55-5920). Although we tried carefully to have the inside zone contain pure magnesite, we observed minor mixing between quartz and magnesite. For the Two-zone and Three-zone columns, two and three plastic tubes with diameters of 7.4 and 6.0 mm were used respectively with the same packing procedure as for the One-zone column.

3.1.4. Determination of porosity and mineral volume fractions

The average porosity was determined by the mineral volume packed in each column. These values were confirmed by a separate calculation on the amount of water used in packing the column to fill the pore space of each column. For the One-zone column, the quartz zone is nominally 100% quartz with relatively little magnesite. However, some quartz was unavoidably dislocated into the magnesite zone during packing, yielding somewhat less than 100% magnesite in the magnesite zone. Based on the packed mass, the porosity was found to be different for the magnesite and the quartz zones. To determine the amount of each mineral in the magnesite zone and the porosity values of the magnesite and quartz zones, the mass and volume balance equations were written for magnesite, quartz, and the average porosity. The unknowns for these equations were the porosity of the two individual zones (ϕ_{Mg} and ϕ_{Qtz}) and the solid volume fraction of magnesite ($VF_{\text{Mg,Mg}}$) and quartz ($VF_{\text{Qtz,Mg}}$) in the magnesite zone. The three mass and volume balance equations, together with the fact that

Table 1
Physical properties of the columns.

Columns	Magnesite (gram)	Quartz (gram)	VF_{Mg} in solids (%) ^a	a_L (cm) ^b	a_L' (cm) ^c	a_T (cm) ^d	Effective perm ($\times 10^{-13} \text{ m}^2$) ^e	Average porosity
Mixed	11.47	76.49	11.37	0.05	0.05	0.005	8.26 (± 0.060)	0.410
Three-zone	11.25	76.86	11.12	–	0.10	–	12.30 (± 0.004)	0.407
Two-zone	11.27	74.58	10.99	–	0.20	–	7.79 (± 0.120)	0.422
One-zone	11.90	78.04	12.00	0.07	0.15	0.004	10.74 (± 0.030)	0.395

^a Calculated value for the solid volume fraction of magnesite (volume magnesite/volume of both quartz and magnesite).

^b a_L is the local longitudinal dispersivity in Eq. (10) for each grid block. Value determined by model fitting as described in text. The two and three-zone columns were not simulated using 2D transport models so no local dispersivity values are reported.

^c a_L' is the global longitudinal dispersivity at the column scale. This was obtained by matching the breakthrough data using average porosity, permeability, and flow rates without considering detailed heterogeneity.

^d a_T is the transverse dispersivity in Eq. (11). The Two and Three-zone columns were not simulated so no dispersivity values are reported.

^e Effective permeability, calculated based on Darcy's law using measured flow rates and pressure gradient. The permeability of the sand column was measured to be $8.7 \times 10^{-13} \text{ m}^2$.

Table 2
Initial and boundary (inlet) fluid composition.^a

Species	Initial Concentrations in the column pore fluid at $t = 0$ (mol/L, except for pH)	Concentrations in the inflowing fluid (mol/L, except for pH)
pH	8.8	4.0
Total Inorganic Carbon (TIC)	3.43×10^{-3} (approximate, close to equilibrium with magnesite)	1.07×10^{-5} (in equilibrium with CO ₂ gas)
Mg(II)	Varies between 0.52×10^{-5} and 1.2×10^{-5} , depending on experimental conditions	0.0
Na(I)	1.00×10^{-3}	1.00×10^{-3} (in dissolution experiment) 1.12×10^{-3} (in tracer experiments)
Cl(-I)	1.00×10^{-3}	1.00×10^{-3}
Br(-I)	0.0	0.0 (in dissolution experiments) 1.20×10^{-4} (in tracer experiments)
Si(VI)	1.00×10^{-5}	1.00×10^{-4}

^a The measured quantities include pH, total aqueous Mg(II), Na(I), Cl(-I), Br(-I), and Si(VI). Concentrations of all individual species were calculated using the speciation calculation in CrunchFlow based on thermodynamic data in Eq3/6 (Wolery et al., 1990).

the summation of $VF_{Mg,Mg}$ and $VF_{Qtz,Mg}$ equals to 1, yield 4 equations for 4 unknowns as shown below.

$$M_{Mg} = V_{Mg} \times (1 - \phi_{Mg}) \times VF_{Mg,Mg} \times \rho_{Mg} \quad (5)$$

$$M_{Qtz} = V_{Qtz} \times (1 - \phi_{Qtz}) \times VF_{Qtz,Qtz} \times \rho_{Qtz} + V_{Mg} \times (1 - \phi_{Mg}) \times VF_{Qtz,Mg} \times \rho_{Qtz} \quad (6)$$

$$\phi_{avg} = \frac{V_{Qtz} \times \phi_{Qtz} + V_{Mg} \times \phi_{Mg}}{V_{tot}} \quad (7)$$

$$VF_{Mg,Mg} + VF_{Qtz,Mg} = 1 \quad (8)$$

In Eq. (5), M_{Mg} is the total magnesite mass added to the column assuming it is strictly in the magnesite zone (gram, measured); V_{Mg} is the total volume of the cylindrical magnesite zone (cm³, i.e., $\pi r_{d,Mg}^2 L$, where $r_{d,Mg}$ is the cylinder radius (0.55 cm) and L is the length of the column (10.50 cm); ρ_{Mg} is the grain density of magnesite (3.10 g/cm³). In Eq. (6), M_{Qtz} is the total mass of quartz (gram, measured), which is primarily in the quartz zone: i.e., $VF_{Qtz,Qtz} = 100\%$ and $VF_{Qtz,Mg}$ is an unknown; V_{Qtz} is the total volume of the quartz zone which can be calculated by difference between the total volume of the column V_{tot} and the volume of the magnesite zone, i.e., $V_{tot} - V_{Mg} = \pi R_d^2 L - \pi r_{d,Mg}^2 L$. Here R_d is the radius of the whole column (1.28 cm). The grain density of quartz, ρ_{Qtz} , is 2.65 g/cm³. In Eq. (7), the average porosity, ϕ_{avg} , equals the ratio of total pore volume of the entire column (i.e., the sum of pore volume in the quartz and magnesite zones) divided by the total volume of the column. The solution to the 4 equations showed that the center zone contained 80.0 vol.% magnesite ($VF_{Mg,Mg} = 0.8$) and 20.0 vol.% quartz ($VF_{Qtz,Mg} = 0.2$) and was packed with a porosity of 54% ($\phi_{Mg} = 0.54$). In contrast, the porosity of the quartz zone was 38% ($\phi_{Qtz} = 0.38$).

3.1.5. Permeability determination

The effective permeability value of each column was calculated using Darcy's law based on measured pressure gradients and flow rates. Another sand column was packed with only quartz to obtain the permeability of the quartz zone. Before this permeability measurement, air bubbles were carefully removed from the pump and the tubes through vacuum and from the columns by flushing at high flow rate. The pressure gradients were measured at flow

rates of 0.3, 0.5, and 1.0 ml min⁻¹ using a Crystal Engineering pressure gauge (XP2i-DP) that can measure a 15 psi differential pressure with a precision of 0.001 psi. To ensure the measurements were made at steady state conditions, each flow rate was kept constant until a differential pressure was stabilized for 15 min with a maximum variation of 0.005 psi.

3.1.6. Tracer tests and dispersivity determination

Tracer tests were conducted to obtain the dispersivity coefficients. Sodium bromide at a concentration of 1.2×10^{-4} mol/L was injected at flow velocities of 3.6 m/d (1.23 ml/min) and 0.36 m/d (0.123 ml/min). With the porosity of the quartz and magnesite zones and the column dimension, the total pore volume can be calculated for each column. The average residence time was then calculated from the total pore volume divided by the flow rate. At 3.6 and 0.36 m/d, the residence time was approximately 16.4 and 164.0 min, respectively. Effluent samples were collected every 0.2 residence times for 2.5 residence times. Effluent bromide concentrations were measured using a Dionex ICS2500 Ion Chromatography (IC). Local longitudinal dispersivities at the grid block scale (a_L) were determined for the Mixed and One-zone column respectively, by assuming no reactions and modeling only transport in the 2D domain using an explicit distribution of magnesite and quartz zones and by matching the bromide breakthrough curves using CrunchFlow (Steefel and Lasaga, 1994). For the One-zone case, porosity values calculated using Eqs. (5)–(8) were applied in the transport modeling, while the permeability ratio and the longitudinal dispersivity were varied as the unknowns. Another “global” dispersivity value (a_L') was obtained by representing the columns as homogeneous 1D columns with the calculated average porosity and permeability. The global dispersivity values, obtained by matching the effluent bromide data, represent those at the column scale.

3.1.7. Total, effective, and interface surface areas

Here we define several surface areas for the reacting mineral magnesite. The *total* reactive surface area of magnesite (A_T) was calculated by multiplying the BET surface

area ($1.87 \text{ m}^2/\text{g}$) and the total mass of magnesite. A_T only depends on the amount of magnesite packed in the column and is a nearly constant value because we purposely packed the same amount of magnesite in all columns. The *effective* surface area (A_e) was defined as the surface area of the magnesite grains that are effectively dissolving – these are the grains that are far from equilibrium. It therefore represents the surface area of the magnesite grains that have local dissolution rates significantly above 0. In this work, values of A_e were calculated by multiplying the magnesite mass that was effectively dissolving (grams) by the measured BET surface area (m^2/g). The mass of the effectively dissolving magnesite were determined based on the output of the reactive transport modeling. Specifically, the effective magnesite was defined as grains having local IAP/K_{eq} values <0.1 . The choice of 0.1 was based on the analysis of the 2D simulations. These results indicate that the local rates in grid blocks with $\text{IAP}/K_{\text{eq}} <0.1$ contribute to the majority of the overall column-scale rates. In addition, other choices of the threshold IAP/K_{eq} such as 0.5 or 0.9 yields similar conclusions with respect to how the rate depends on A_e , as will be discussed later. Values of A_e (and A_e/A_T) depend on the spatial distribution of the magnesite and on the flow rate. The ratio A_e/A_T represents the fraction of magnesite that is “effectively” dissolving at a significant rate. A third surface area, the *interface* surface area A_I , was defined as the amount of the effective surface area that is at the magnesite–quartz interface. For the Mixed column, it was taken to be the same as the total effective magnesite surface area because all the magnesite grains were assumed in that column to be surrounded by quartz. For the One-zone column, it was calculated as the effective surface area of magnesite grains lying within the first 2 grid blocks from the magnesite–quartz interface. In other words, the quartz–magnesite interface was defined to be two grid blocks thick. As such, the ratio of A_I/A_e represents the proportion of the effective surface area that is at the immediate interface of the zones of magnesite and quartz. This ratio emphasizes the importance of the magnesite lying within the magnesite–quartz interface in contributing to the effective surface area.

3.1.8. Flow through dissolution experiment

The experiments were operated at room temperature between 22 and 25 °C with the influent solution flowing upward. The experiment was run with velocities of 0.36 and 3.6 m/d to represent medium to fast flow velocities of ground water in the natural subsurface (Newell et al., 1990). Due to the relatively short time scale of the dissolution experiments, the total magnesite surface area was assumed to remain constant over time and the same columns were used for both flow velocities. For each flow velocity, duplicate flow through experiments were run. Before each experiment, the columns were flushed with an initial solution at a pH of 8.8 at a flow rate of 18.0 m/d to wash out the dissolved Mg(II) initially in the columns and to maintain relatively consistent initial conditions across different columns and different experiments. Although the permeability values differ, we used a syringe pump to maintain constant flow rates for all four columns during the experiments.

The inlet solution contained 10^{-3} M NaCl with pH adjusted to 4.0 using HCl. The inlet reservoir solution was maintained in equilibrium with the partial pressure of CO_2 in the atmosphere. The inlet and initial aqueous composition are shown in Table 2. For each column, 14 effluent samples were collected for 8 residence times at a frequency of 3 times per residence time for the first 3 residence times and once per residence time for the final 5 residence times. All samples were filtered through $0.22 \mu\text{m}$ filters, collected in polypropylene plastic vials, and acidified with one drop of 2% HNO_3 to prevent precipitation. Effluent samples were analyzed using a Perkin-Elmer Optima 5300 Inductively Coupled Plasma Atomic Emission Spectrometry (ICP-AES).

3.2. Reactive transport modeling

Two-dimensional (2D) reactive transport modeling was carried out using the code CrunchFlow for the Mixed and One-zone columns to represent one slice of each column. Reactive transport modeling has been used to understand various processes in a wide range of applications (Lichtner, 1985; Van Cappellen and Gaillard, 1996; Steefel et al., 2005; Li et al., 2006; Laverman et al., 2007; Chang et al., 2011), including, for example, mineral dissolution (Maher et al., 2006; Molins et al., 2012; Moore et al., 2012), chemical weathering (Hausrath et al., 2008; Maher, 2011), ion exchange (Singha et al., 2011), and microbe-mediated redox reactions (Li et al., 2010; Druhan et al., 2012; Godderis et al., 2013). In particular, it has been used to simulate coupled processes in physically and chemically heterogeneous subsurface (Li et al., 2011).

3.2.1. Reactions and species

In the column experiments, in addition to the magnesite dissolution as the kinetically controlled reaction, other instantaneous aqueous speciation reactions occur. The species include Mg^{2+} , MgHCO_3^+ , $\text{MgCO}_3(\text{aq})$, H_2CO_3^0 , HCO_3^- , CO_3^{2-} , H^+ , OH^- , Na^+ , Cl^- , and Br^- . A reactive transport formulation typically partitions the species into primary and secondary species. The primary species compose the key species that determine the chemistry of the system, while the secondary species can be written in terms of primary species using the mass action laws of the instantaneous reactions (Lichtner, 1985, 1996). Here Mg^{2+} , HCO_3^- , H^+ , Na^+ , Br^- and Cl^- were assumed to be the primary species. All other species were set as secondary species.

All reactions and their thermodynamic and kinetic parameters are shown in Table 3. The reaction equilibrium constants were derived from the EQ3/6 database (Wolery et al., 1990) except that of magnesite. We used the same thermodynamic and rate constants for magnesite dissolution as in our previous study (Salehikhoo et al., 2013). We did not need to adjust any of these to match data. In comparison with literature values, the log (equilibrium constant) we used for magnesite solubility ($\log K_{\text{sp}} = -7.83$) is higher than the reported value -8.02 calculated from SUPCRT92 (Johnson et al., 1992) and that reported in Morse et al. (2007), resulting in a solubility which is higher by a factor of 1.58 (Morse et al., 2007). This value is very close

Table 3

Chemical reactions and parameters used in the model.

	Log K_{eq}	k (mol/m ² /s)	SSA (m ² /g, BET, measured)
<i>Aqueous speciation (at equilibrium)</i>			
$H_2O \rightleftharpoons H^+ + OH^-$	−14.00	—	—
$H_2CO_3^0 \rightleftharpoons H^+ + HCO_3^-$	−6.35	—	—
$HCO_3^- \rightleftharpoons H^+ + CO_3^{2-}$	−10.33	—	—
$MgHCO_3^+ \rightleftharpoons Mg^{2+} + HCO_3^-$	−1.04	—	—
$MgCO_3(aq) \rightleftharpoons Mg^{2+} + CO_3^{2-}$	−2.98	—	—
<i>Kinetic reactions (log K value is log K_{sp} value)</i>			
$MgCO_3(s) + H^+ \rightleftharpoons Mg^{2+} + HCO_3^-$	—	6.20×10^{-5}	1.87
$MgCO_3(s) + H_2CO_3^0 \rightleftharpoons Mg^{2+} + 2HCO_3^-$	—	5.25×10^{-6}	1.87
$MgCO_3(s) \rightleftharpoons Mg^{2+} + CO_3^{2-}$	−7.83	1.00×10^{-10}	1.87

to the $\log K_{sp}$ value of -7.99 ± 0.15 reported at 50 °C (Benezeth et al., 2011). Our rate constants and surface area are also in general higher than those reported in Chou et al. (1989), reflecting the higher reactivity of our samples.

3.2.2. Reactive transport equations

The reactive transport equations were solved for the total concentration of all primary species. For example, the equation for the total concentration of the primary species Mg(II) is the following:

$$\frac{\partial(c_{Mg(II)})}{\partial t} = D_L \frac{\partial^2 c_{Mg(II)}}{\partial z^2} + D_T \frac{\partial^2 c_{Mg(II)}}{\partial x^2} - v_z \frac{\partial c_{Mg(II)}}{\partial z} - v_x \frac{\partial c_{Mg(II)}}{\partial x} + r_{MgCO_3} \quad (9)$$

where $c_{Mg(II)}$ is the total concentration of all Mg^{2+} -containing species (mol/m³), v is the flow velocity (in all directions) with the z direction being the main flow direction (m/s), t is time (s), and A is the magnesite surface area per unit pore volume (m²/m³ pore volume). The value of r_{MgCO_3} (mol/s) is the dissolution rate represented by Eq. (4) per unit pore volume. D_L and D_T are longitudinal and transverse dispersion coefficients (m²/s) given by

$$D_L = D^* + a_L v_z \quad (10)$$

$$D_T = D^* + a_T v_x \quad (11)$$

Here D^* is the effective diffusion coefficient in porous media (m²/s), a_L and a_T are the longitudinal and transverse dispersivity (m). For non-reactive tracer transport modeling to determine dispersivities, a similar equation to Eq. (9) was solved except without the reaction term. The D^* was calculated using Archie's law (Roy and Tarafdar, 1997) by multiplying the molecular diffusion coefficient in water times the value of the porosity, assuming a cementation factor of 1.0. Although the diffusion coefficients for individual aqueous species vary, we used a median value of 6.34×10^{-6} cm²/s from among the diffusion coefficient of all species.

3.2.3. Numerical simulation

The 2D domain was evenly discretized into 100×25 grid blocks with an approximate resolution of 1×1 mm². This resolution was chosen because it was the lowest resolution that generated the same outputs as those using higher resolution. Measured porosity, permeability, and flow rates

and estimated a_L values from the tracer breakthrough curves were used in the reactive transport model. The reaction thermodynamic and kinetic parameters are the same as those we used in our previous study (Salehikhoo et al., 2013) and are shown in Table 3. The numerical simulation generates the spatial and temporal evolution of the aqueous concentrations. For the Mixed column, using the measured and estimated set of parameters fit the Mg breakthrough curves well. For the One-zone column, the transverse dispersivity a_T was adjusted to match the breakthrough data.

3.2.4. Representation of the 3D columns by 2D domain

The Mixed and the One-zone columns are symmetric in the radial direction and were numerically simulated for their 2D cross-sectional domains. The Mixed column is physically homogeneous so the concentrations and flow rates are spatially uniform across the cross-section in the top-down 2D radial dimension. For the One-zone column, however, due to the heterogeneity in porosity, permeability, and mineral distribution, both the flow fields and the geochemical conditions vary in the radial direction. In order to compare 2D simulation results with the measured data from the actual 3D column, the spatial variation in the radial direction must be taken into account. Fig. 1B shows a schematic representation of the One-zone case plotted in the radial direction. The numerical simulation was completed on the radial cross section which was divided into 25 grid blocks, with the middle 11 grid blocks being the magnesite blocks and the outside 14 grid blocks being the quartz blocks. The total radial cross sectional area of the 3D column $A_{c,T}$, total flow rate Q_T , and average effluent concentrations $C_{effluent}$ can be expressed through the following equations:

$$A_{c,T} = \sum_{i=1}^n A_{c,i} = \sum_{i=1}^n \pi (r_{d,i}^2 - r_{d,i-1}^2) \quad (12)$$

$$Q_T = \sum_{i=1}^n q_i = \sum_{i=1}^n v_i A_{c,i} \quad (13)$$

$$C_{effluent} = \frac{\sum_{i=1}^n c_i q_i}{Q_T} \quad (14)$$

Here $r_{d,i-1}$ and $r_{d,i}$ are the radius of the $(i-1)$ th and i th circle from the center of the domain (cm), $A_{c,i}$, q_i , v_i , and c_i , are the corresponding cross-sectional area (cm²), flow rate

(cm³/day), flow velocity (cm/day), and concentration (mol/L) eluting from the annulus between radius $r_{d,i-1}$ and $r_{d,i}$, respectively, Q_T is the total flow rate (cm³/day), and C_{effluent} is the effluent concentration averaged over the radial cross section (mol/L). Eq. (14) says that the total effluent concentration is the flow rate-averaged concentration from individual annulus.

3.3. Dissolution rates at different scales

3.3.1. Local dissolution rates $r_{\text{MgCO}_3,i}$

The local bulk magnesite dissolution rate (mol/s) $r_{\text{MgCO}_3,B,i}$ in each grid block i depends on local aqueous chemistry and local magnesite surface area. It was calculated by using Eq. (4) and the local concentrations in each grid block i predicted by the model.

3.3.2. Column-scale dissolution rates

The columns typically reach steady state, where the concentrations do not vary with time, after a couple of residence times. The steady-state column-scale reaction rate $R_{\text{MgCO}_3,B}$ (mol/s) was calculated as follows:

$$R_{\text{MgCO}_3,B} = Q_T [C_{\text{Mg(II),out}} - C_{\text{Mg(II),in}}] = \sum_{i=1}^n r_{\text{MgCO}_3,i} \quad (15)$$

Here Q_T is the total flow rate (m³/s), $C_{\text{Mg(II),out}}$ and $C_{\text{Mg(II),in}}$ are the effluent and influent Mg(II) concentrations, respectively (mol/L), $r_{\text{MgCO}_3,i}$ is the rate in grid block i determined based on Eq. (4). The first equation is simply a statement of mass balance for the column and was calculated strictly from measured quantities. The second equation says that the overall rates at the column scale is the summation of local rates at the grid block scale calculated using CrunchFlow model results. The two ways of calculating column scale rates are equivalent.

If the column-scale bulk rates in Eq. (15) is normalized by BET surface area A_T , we obtain R_{MgCO_3} in units of mol/m²/s as follows:

$$R_{\text{MgCO}_3} = \frac{R_{\text{MgCO}_3,B}}{A_T} \quad (16)$$

4. RESULTS AND DISCUSSION

4.1. Porosity and permeability

All columns have similar average porosity with similar mass of magnesite and quartz, as shown in Table 1. The average porosity of the 4 columns varies between 0.395 and 0.422, with the One-zone and Two-zone columns having the lowest and highest porosity, respectively. The effective permeability values vary between 7.79 and 10.74×10^{-13} m² (Table 1). The measured permeability of the pure sand column was 8.70×10^{-13} m². These are within the reported range of 8.2×10^{-14} to 4.6×10^{-11} m² for unconsolidated sand with a medium grain size range of 0.25–0.50 mm (Domenico, 1990). The differences among columns are likely caused by differences in texture and particle geometries of the two minerals. Among the 4 columns, the average porosity values do not correspond to the effec-

tive permeability values. For example, although the Two-zone column has the highest average porosity of 0.422, it has the lowest effective permeability of 7.79×10^{-13} m². The different effective permeability values indicate that spatial zonation – chemical heterogeneity – can result in different hydrological properties.

Although the same grain sizes for magnesite and quartz were used with the intention of generating a physically homogeneous column, the porosity of the magnesite and quartz zones in the One-zone column were calculated to be 0.54 and 0.38 for the magnesite and quartz zones, respectively. With different porosity, it is expected that they have different permeabilities. With the measured effective permeability value of 10.74×10^{-13} m² for the entire column and a sand-column permeability of 8.7×10^{-13} m², the permeability values of the magnesite zone can be estimated to be 20.2×10^{-13} m² assuming the effective permeability is the cross sectional area-weighted average of individual zones. This gives a permeability ratio of approximately 2.2 for magnesite versus quartz zones. However, this value leads to early breakthrough and overestimation of Br concentration during the tracer modeling. This indicates either that the permeability measurement was inaccurate or that the effective permeability was not adequately calculated by cross-sectional area-weighting of the permeability of the individual zones (or both). As an alternative, the permeability ratios of the two zones were determined together with the longitudinal dispersivity value by using the measured overall flow rate, effective permeability, and tracer breakthrough curves as constraints. The best match was obtained when a permeability ratio of 1.2 was used. We did not use a porosity–permeability relationship because such relationships are typically sample-specific and largely depend on the details of pore structure (Bernabe and Bruderer, 1998; Bernabe et al., 2003, 2011; Colon et al., 2004). Even with the same mineralogy, porosity–permeability relationships can vary significantly from one system to another.

4.2. Dispersivity

Despite the differences in effective permeability, the breakthrough data nearly overlapped within the measurement error (note error bars), indicating similar dispersive characteristics across the columns, as shown in Fig. 2. The similarity in the mean breakthrough times confirmed similar average porosities (0.395–0.422) for all columns. The data show slightly longer tails and some non-Fickian behavior as compared to predictions based on the standard Advective Dispersion Equations (ADE). The Mixed column is the closest to the standard ADE curve, primarily due to its homogeneous properties. The Two-zone column shows the longest tail and the largest extent of non-Fickian behavior. Interestingly, this column also has the largest porosity and lowest measured effective permeability values. Local longitudinal dispersivity (a_L) values were determined to be 0.05 and 0.07 cm for the Mixed and One-zone columns, respectively. All these values are within the range reported for grid-block spatial scales of 1 mm in the literature (Gelhar et al., 1992; Hunt et al., 2011).

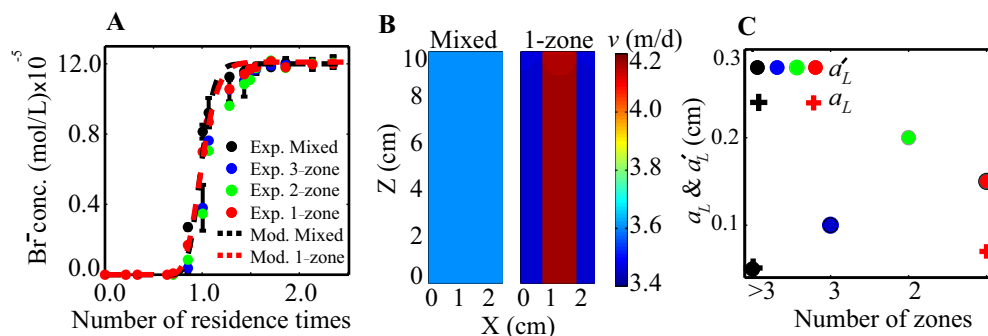


Fig. 2. (A) Experimental (symbols) and modeling (lines) output depicting breakthrough curves for the non-reactive tracer bromide. The symbols are the experimental data with error bars from duplicate flow-through experiments. The dashed lines are the model output for the Mixed and One-zone columns. The Darcy flow velocity was 3.6 m/d (flow rate 1.23 ml/min) with an average residence time of 16.4 min. The breakthrough curves at 0.36 m/d were also measured. They were almost identical to curves in this figure and are not shown; (B) Comparison of the predicted spatial distribution of local flow velocities in the Mixed (left) and 1-zone columns (right), where *X* is the column cross-sectional direction and *Z* is the vertical upward-flowing direction; (C) global and local dispersivity (*a*_L' and *a*_L) as a function of the number of zones. The ">3" case is for the Mixed column. It shows that the zoned columns (Three-zone, Two-zone, One-zone) in general have higher global dispersivity values than the Mixed column. Note that for the Mixed column, local and global dispersivity overlap. (For interpretation of the references to color in this figure legend, the reader is referred to the web version of this article.)

To match the bromide breakthrough data of the One-zone column, the permeability ratio between the magnesite and the quartz zones turned out to be a critical parameter. Fig. 2C compares the spatial distribution of flow velocities calculated in the Mixed and One-zone columns using the permeability ratio of 1.2. The Mixed column is homogeneous and has the same flow velocity everywhere, 3.6 m/d. For the One-zone column, due to the difference in permeability values of the magnesite and the quartz zones, the flow velocity in the magnesite zone is 4.2 m/d, i.e., 1.2 times that of the 3.4 m/d in the quartz zone.

Although the 2D reactive transport modeling was carried out only for the Mixed and One-zone cases, the column-scale (global) longitudinal dispersivity values (*a*_L') were determined for all 4 columns. This was done by non-reactive transport modeling to match the tracer breakthrough data and by assuming homogeneous 1D columns with average porosity and measured effective permeability values. As shown in Table 1 and Fig. 2C, the global dispersivity values were determined to be 0.05, 0.10, 0.20, and 0.15 cm for the Mixed, Three-zone, Two-zone, and One-zone columns, respectively. As expected, these values are larger than the local dispersivity values because dispersivity values depend on spatial scales (Gelhar et al., 1992; Hunt et al., 2011). In addition, the global dispersivity values of all three zonation columns (Three-zone, Two-zone, and One-zone) are larger than that in the Mixed column, indicating that even at the 10 cm spatial scale, the global column-scale dispersivity values are affected by spatial heterogeneities.

For the Mixed column, both tracer and Mg(II) breakthrough curves are not sensitive to the transverse dispersivity so a transverse-to-longitudinal dispersivity ratio (*a*_T/*a*_L) of 0.1, typical for this type of system, was assigned to obtain a *a*_T value of 0.005 cm (Gelhar et al., 1992). For the One-zone column, the transverse dispersivity was determined to be 0.004 cm by matching the Mg(II) breakthrough curves at 3.6 m/d. This leads to an *a*_T/*a*_L ratio of 0.06, close

to a ratio of 0.1. These values fall in the typical range for longitudinal and transverse dispersivity values determined at a spatial scale of grid blocks (Gelhar et al., 1992; Hunt et al., 2011).

4.3. Mg breakthrough curves

The Mg breakthrough curves are shown in Fig. 3. Under each flow condition, the effluent Mg concentrations increased from the initial to steady state concentrations after about three residence times. At 3.6 m/d, the steady-state concentration from the Mixed column was the largest (1.61×10^{-4} mol/L), i.e., approximately 1.6, 1.7, and 1.9 times the concentrations observed for the other three columns (Three-, Two- and One-zone respectively). The difference was relatively small among the zonation columns (Three, Two, and One-zone columns). Similarly, at 0.36 m/d, the Mixed column had the highest Mg(II) concentration (2.60×10^{-4} mol/L). At this flow velocity, the residence time was 10 times longer, allowing much longer water–magnesite contact. This resulted in a higher Mg(II) concentration than that at 3.6 m/d. The Mg(II) concentrations from the Mixed column were about 1.5, 1.6, and 1.7 times those in the Three, Two, and One-zone columns, respectively. The rates in the zoned columns once again remain relatively similar.

4.4. Column-scale dissolution rates

Fig. 4A shows the column-scale rates calculated using Eq. (15) based on the steady-state effluent Mg(II) concentrations. The column-scale rates are highest in the Mixed column and decrease with decreasing number of magnesite zones. Fig. 4B shows the ratios of the column-scale rates in the Three-, Two-, and One-zone columns relative to that in the Mixed column. The ratio values are all lower than unity, indicating lower rates in the zonation columns compared to those in the Mixed column. The deviation of the

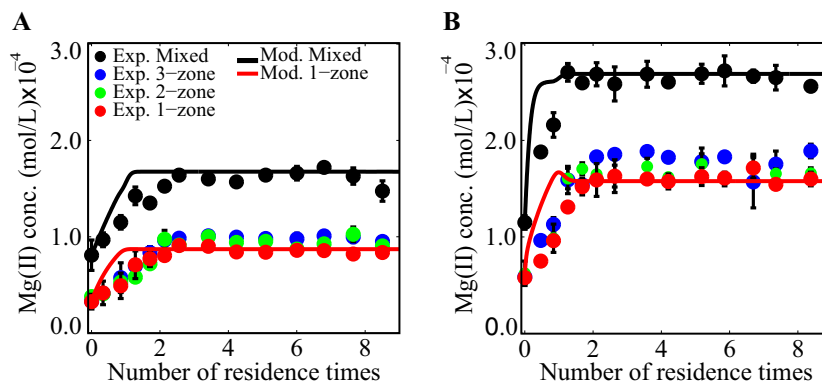


Fig. 3. Experimental breakthrough data (symbols) and model output (solid lines) of Mg(II) concentration under flow velocities of (A) 3.6 m/d and (B) 0.36 m/d. The Mixed column has the highest effluent Mg(II) concentrations under both flow conditions. The zonation columns have lower Mg(II) concentrations than those from the Mixed column, indicating lower dissolution rates. Among the Three-zone, Two-zone, and One-zone columns, the differences are relatively small.

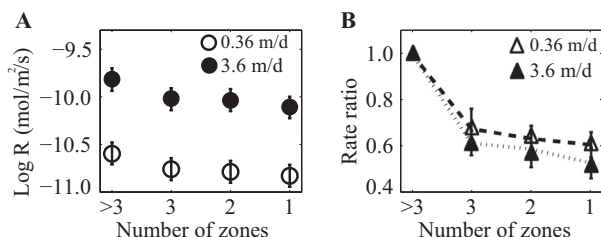


Fig. 4. (A) The logarithm of R_{MgCO_3} (i.e., the column dissolution rate normalized by the total surface area A_T) plotted as a function of the number of magnesite zones; (B) Ratio of the rates of the zonation columns versus that of the Mixed column as a function of the number of zones. The symbol “>3” represents the Mixed column. The largest difference is about a factor of 2 between the rates in the Mixed column and that in the One-zone column observed at the higher flow velocity of 3.6 m/d.

ratio from 1 is slightly lower with the lower flow velocity of 0.36 m/d, indicating smaller differences among the columns. This is likely due to the longer residence time and the increasing importance of diffusion in homogenizing the concentration fields at the slower flow rate. In addition, lower flow velocities also lead to local equilibrium conditions, which make the reaction kinetics less relevant because a higher proportion of the fluid in the column is equilibrated with magnesite under these conditions.

4.5. Local geochemistry and dissolution rates

To understand the difference in column-scale rates, Fig. 5 shows the predicted 2D steady-state spatial profiles of Mg(II) concentration, pH, IAP/K_{eq} , and local dissolution rates for the Mixed and One-zone columns using the set of parameters that matched the bromide and Mg breakthrough curves. The top (5A–5D) and the bottom figures (5E–5H) are for 3.6 and 0.36 m/d, respectively. Comparing the two flow velocities, the lower flow velocity results in higher Mg(II), pH, and IAP/K_{eq} due to an order of magnitude longer residence time. This is consistent with the larger effluent Mg concentration in Fig. 3.

In the Mixed column (the left figure of each pair), because magnesite was homogeneously distributed, dissolution occurred everywhere. The dissolution increases the pH, Mg(II), and IAP/K_{eq} values along the main flow direction. Correspondingly, the local dissolution rates decrease by approximately 2–5 orders of magnitude, depending on the flow velocity. The magnesite grains in the Mixed column can be considered as being present in an infinite number of small zones which experience the least mass transport limitation. In the One-zone column, however, magnesite grains are concentrated in the middle zone. Like the Mixed column, the Mg(II) concentration, pH, and IAP/K_{eq} increase significantly in the magnesite zone toward the outlet. They also increase toward the center of the magnesite zone, leading to local equilibrium conditions with IAP/K_{eq} close to 1. The local dissolution rates in these local equilibrium regions are 2–4 orders of magnitude lower than the maximum dissolution rates close to the inlet and those at the magnesite–quartz interface. The center of the zone is essentially non-reactive. In other words, only the magnesite grains close to the inlet and at the magnesite–quartz interface are effectively dissolving. Likewise, the Mg(II) concentration in most of the quartz zone is close to zero except right at the magnesite–quartz interface. The concentration gradients and the distribution of rates and IAP/K_{eq} values in the x direction indicate that the overall magnesite dissolution is transport limited, i.e., the rate depends on how fast the dissolved Mg(II) and carbonate are transported out of the local equilibrium-controlled magnesite zone into the dilute quartz zone. In effect, the mineral zonation creates mass transport limitation in the direction that is perpendicular to the main flow. This does not occur in the Mixed column which was assumed to be perfectly well mixed. Of course, in real systems small clusters of reactive mineral could be transport-limited at the scale of the cluster size. Note also that under both flow velocity conditions, the majority of the magnesite zone in the One-zone column contains fluid within the pH range of 8–10, indicating the dominance of reaction (3) under such conditions.

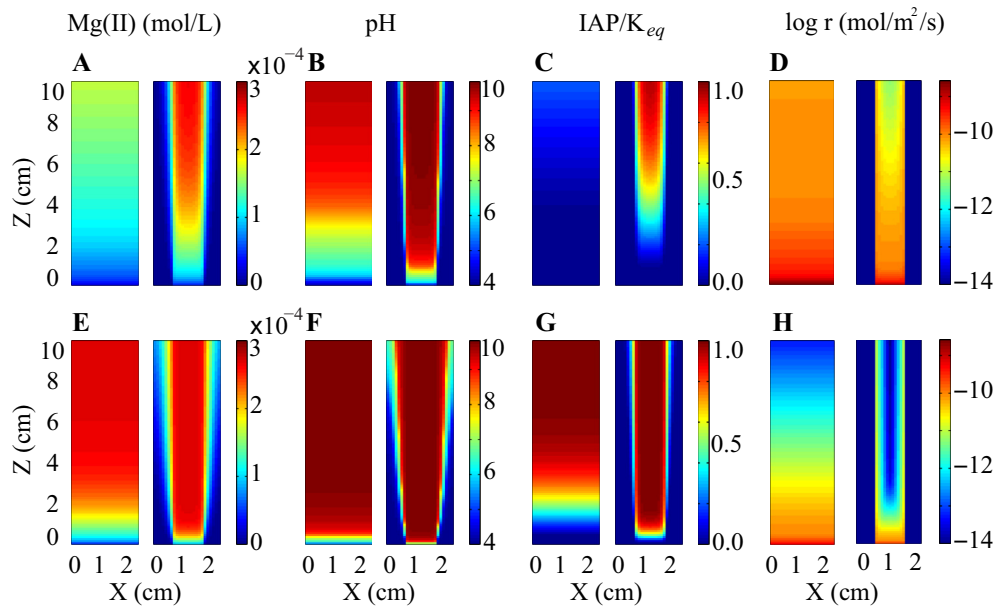


Fig. 5. Predicted 2D spatial profiles of aqueous geochemistry and local dissolution rates under steady state conditions for the Mixed and One-zone columns at flow velocities of 3.6 m/d (top) and 0.36 m/d (bottom). Colors are for Mg(II) concentration, pH, IAP/ K_{eq} , and $\log r$ as shown in the color bar at the right of each panel. Flow was from the bottom to the top. For each pair of figures, the left figure is for the Mixed column and the right for the One-zone column. (A and E): Mg(II), (B and F): pH, (C and G): IAP/ K_{eq} , (D and H): $\log r$, the local area-normalized magnesite dissolution rate calculated for each grid block ($\text{mol}/\text{m}^2/\text{s}$). X is the position across the column and Z is the distance along the column from the inlet. As shown in panels C and G, for the higher flow velocity of 3.6 m/d, only the One-zone system reaches equilibrium (IAP/ K_{eq} values approach 1, color-coded as red) and this occurs only at the center of the column toward the outlet. At the lower flow velocity of 0.36 m/d, almost the whole magnesite zone is at equilibrium in both columns except at the inlet, or in the outer zone toward the inlet in the One-zone column. Under both flow velocities, the magnesite zone in the One-zone column is characterized by a much higher local Mg(II), pH, IAP/ K_{eq} , and correspondingly lower dissolution rates, indicating mass transport limitation. (For interpretation of the references to color in this figure legend, the reader is referred to the web version of this article.)

4.6. Effects of transverse dispersivity

For the Mixed column, the model output is not sensitive to the transverse dispersivity a_T because there is no concentration gradient in the direction perpendicular to the main flow. For the One-zone column, however, a_T was found to be the key parameter that controls the fit to the Mg(II) breakthrough data. This is expected because magnesite dissolution reaches equilibrium inside the middle zone and the rate of dissolution is limited by rates of mass transport between the two zones. To illustrate the effects of transverse dispersivity, we simulated additional cases by varying the a_T value while keeping all other parameters constant, including the longitudinal dispersivity value a_L . Fig. 6A shows the comparison of three cases with three different a_T values and their corresponding effluent Mg(II) concentrations for the One-zone column. Relatively low a_T values of 4.0×10^{-4} cm leads to much lower effluent Mg(II) concentrations, while a relatively high value of 4.0×10^{-2} cm results in the same effluent Mg(II) as that in the Mixed column. The medium value of 4.0×10^{-3} cm fits the Mg(II) breakthrough data from the One-zone column.

As shown in Fig. 6B, a larger a_T value (4.0×10^{-2} cm) results in faster mass transport of dissolution products out of the magnesite zone, which significantly enlarges the zone with non-zero Mg(II) concentration. This in turn leads

to larger column volumes with smaller IAP/ K_{eq} values and higher local dissolution rates that occur without reaching local equilibrium. In effect, all magnesite is dissolving. In contrast, with a small a_T value (4.0×10^{-4} cm), Mg(II) that was released by dissolution essentially was “confined” to the magnesite zone due to the small mass transport rates at the magnesite–quartz interface. This results in a large local equilibrium volume in the middle of the magnesite zone: in this volume, local dissolution rates were 2–3 orders of magnitude lower than the maximum local rates. In effect, as the transverse dispersivity decreases, dissolution becomes more restricted to only the magnesite grains at the magnesite–quartz interface and close to the inlet. As such, the transverse dispersivity, essentially a measure of the mass transport rate at the interface, controls the amount of effectively-dissolving magnesite.

As discussed in the methodology section, the *effective* surface area (A_e) was defined as the surface area of the magnesite grains bathed in porefluids with local IAP/ K_{eq} values lower than 0.1. The ratio A_e/A_T represents the proportion of the total surface area that is effectively dissolving. The *interface* surface area A_I was defined as the effective surface area that is close to the magnesite–quartz interface. For the Mixed column, it was taken to be the same as the effective magnesite surface area, i.e., assuming perfect mixing such that all magnesite grains are surrounded by quartz grains.

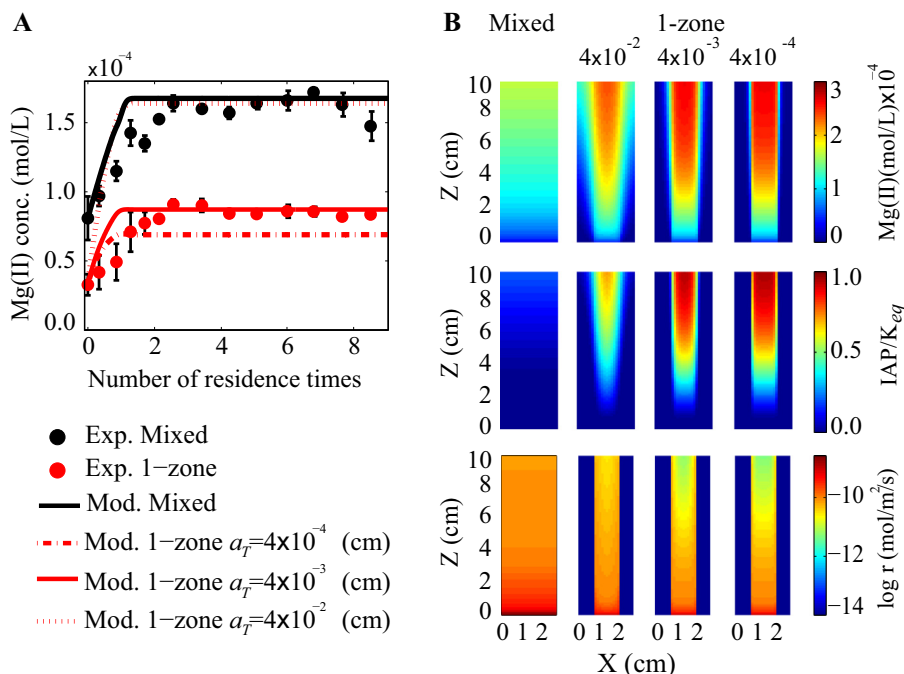


Fig. 6. (A) Sensitivity of the calculated breakthrough curves (lines) to the assumed values of the transverse dispersivity a_T shown in comparison to measured values (symbols); (B) Spatial profiles of dissolved Mg(II) (first row), IAP/ K_{eq} (second row), and local dissolution rates (third row) in the Mixed column (the first left one in each row) and in the One-zone column with three transverse dispersivity values (a_T) of 4.0×10^{-2} , 4.0×10^{-3} , and 4.0×10^{-4} cm. These are for the flow velocity of 3.6 m/d. The transverse dispersivity determines the rates of mass transport, the local equilibrium regions, the effective surface area, and therefore the overall column-scale dissolution rates.

For the One-zone column, it was calculated as the effective surface area that is within the first 2 grid blocks from the magnesite–quartz interface. The ratio of A_I/A_e represents the proportion of the effective surface area lying within the magnesite–quartz interface and is a measure of the importance of the interface magnesite in contributing to A_e .

Under one flow condition, the transverse dispersivity controls A_e , A_I , and column-scale bulk rates $R_{MgCO_3,B}$, as shown in Fig. 7. The surface area and rates were obtained by systematically varying the value a_T while maintaining all other parameters constant. Fig. 7A shows that although A_T remains a constant value of 22.5 m^2 for all cases, A_e and A_I increase with increasing a_T values. The A_e values vary between 16% and 27% of the A_T values. When a_T values are smaller than 10^{-3} cm, A_e and A_I increase slowly, as shown in Fig. 7A, indicating the dominance of the diffusion process with constant diffusion coefficient, as implied in Eq. (11). Under this condition, the A_e and A_I values are at their lower limit and they do not increase quickly with increasing a_T values. Under these low a_T value conditions, the magnesite grains in the interface contribute to about 60% of the A_e , as shown in Fig. 7B. When a_T values are larger than 10^{-3} cm, both A_e and A_I increase faster, indicating that mass transport is faster and the dispersion term dominates in Eq. (11). Under these conditions, the magnesite grains in the interface contribute about 61–72% of the A_e . The magnesite grains close to the inlet contribute the rest of the A_e .

Fig. 7C shows the corresponding column-scale bulk rates ($R_{MgCO_3,B}$, mol/s) as a function of A_e and A_I with different a_T values. As shown before, A_T is a constant while

the rates vary from 1.37×10^{-9} to 3.36×10^{-9} (mol/s). Thus, column-scale bulk rates do not depend on the total surface area. Instead, the rates depend strongly on A_e and A_I . The importance of the transverse dispersivity echoes the importance of transverse mixing that has been discussed in modeling and experimental studies for bimolecular reactions where two different types of waters containing aqueous reactants A and B were mixed at the interface and transformed into an aqueous product C (Tartakovsky et al., 2008; Zhang et al., 2010; Hochstetler et al., 2013).

4.7. Column-scale bulk rates as a function of effective and interface surface area (A_e and A_I)

With the constant a_T value for the columns, the effective and interface surface areas are a function of the magnesite spatial distribution and flow rates, as shown in Fig. 8A. The Mixed and the One-zone columns were modeled and their A_e and A_I values were directly calculated from the model output as discussed before. For the Two-zone and Three-zone columns, the A_e and A_I values were obtained by using the ratio of their column-scale rates to the corresponding rate of the Mixed column under the same flow rate. For example, for the Two-zone column, at 3.6 m/d, its rate is approximately 60% of that of the Mixed column. As a result, we approximate the A_e and A_I to be 60% of the corresponding surface area values of the Mixed column at 3.6 m/d. This is based on the observation that the column-scale strongly depend on the A_e value for the One-zone column, as shown in Fig. 7C.

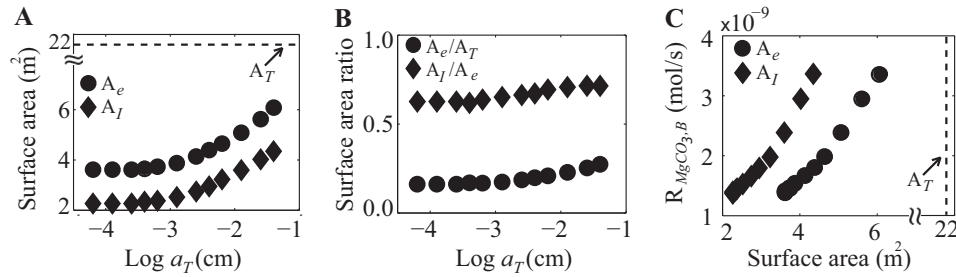


Fig. 7. (A) Values of the effective (A_e) and interface surface area (A_I) calculated for different assumed values of a_T for the One-zone column. Also shown is the total magnesite BET surface area of 22.5 m², which is a measured quantity that does not vary with a_T ; (B) Surface area ratios (A_e/A_T or A_I/A_e) as a function of a_T values; (C) Column-scale bulk rates ($R_{MgCO_3,B}$, mol/s) as a function of the different types of surface area corresponding to the different a_T values in A. The surface area values and rates were obtained by varying a_T in the model for the One-zone column while maintaining all other parameters the same.

The trend of A_e and A_I as a function of the number of zones shown in Fig. 8A is very similar to that of the column-scale rates shown in Fig. 4. It is notable that the A_I values are very close to the A_e values, i.e., between 60% and 72% of the effectively dissolving surface lies within 2 grid blocks from the magnesite–quartz interface. It is also interesting to note that although the BET surface area remains a constant 22.5 m² in all columns, A_e/A_T varies between 18% and 66% at the higher flow rate while A_e/A_T varies between 2% and 8% at the slower flow rate. In effect, although the total surface area of magnesite remains the same, decreasing the flow rate essentially reduces the amount of dissolving magnesite, and therefore results in lower column-scale dissolution rates.

The column-scale rates in units of mol/s strongly depend on values of A_e and A_I as shown in Fig. 8B. The regression line for rates (mol/s) as a function of A_e is $R_{MgCO_3,B}$ (mol/s) = $10^{-9.56} A_e$ with an R^2 of 0.88, while the regression line for rates (mol/s) as a function of A_I is $R_{MgCO_3,B}$ (mol/s) = $10^{-9.22} A_I$ with an R^2 of 0.83. With the steady state pH values around 8–10 for most of column in the magnesite zones, one would expect that reaction (3) would dominate. Under well-mixed conditions, the rate law for reaction (3) is $R_{MgCO_3,B}$ (mol/s) = $10^{-10} A_T$. The local rate constant of 10^{-10} (mol/m²/s) is remarkably close to the value of

$10^{-9.56}$ inferred from Fig. 8B for the relationship between $R_{MgCO_3,B}$ and A_e . This indicates that the rate constant measured under well-mixed laboratory conditions is only applicable to the column-scale reaction rate if we use A_e , the surface area of magnesite in the column bathed by non-equilibrated fluids. The laboratory constant is not applicable if we instead use A_T , the total surface area. Since it is the norm for most reactive transport model treatments of natural systems to use a surface area that is orders-of-magnitude smaller than the total surface area to achieve good fits between models and observations (Moore et al., 2012), we hypothesize that a large fraction of the surface area in natural systems is bathed in equilibrated fluids where reaction rates are minimal.

4.8. Column-scale rates and Damkohler number

To compare the rates in the flow-parallel zonation columns from this work with those from our previous study using Mixed and flow-transverse One-zone columns, we introduce the dimensionless Damkohler number that we defined previously (Salehikhoo et al., 2013):

$$Da_I = \frac{\tau_{adv}}{\tau_r} = \frac{\frac{L}{v}}{\frac{V_p C_{eq,Mg}}{R_{MgCO_3,B}}} = \frac{LR_{MgCO_3,B}A_T}{vV_p C_{eq,Mg}} \quad (17)$$

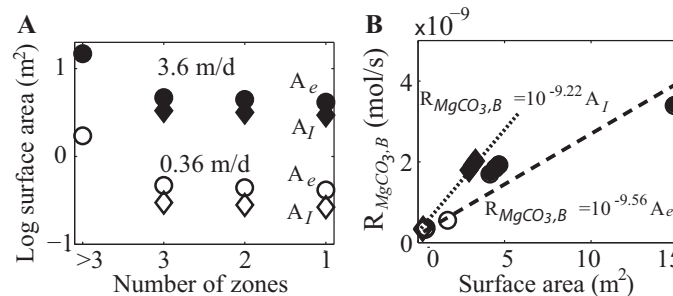


Fig. 8. (A) The logarithm of calculated effective (A_e) or interface (A_I) surface area as a function of the number of zones under different flow rate condition. Filled symbols are for 3.6 m/d, open symbols are for 0.36 m/d, circles are for effective surface area A_e , diamonds are for interface surface area A_I ; (B) Column-scale bulk dissolution rate $R_{MgCO_3,B}$ (mol/s) for different flow rate in different zonation experiments plotted as a function of A_e and A_I as shown by symbol definitions in (A). The Mixed column is shown as >3 zones.

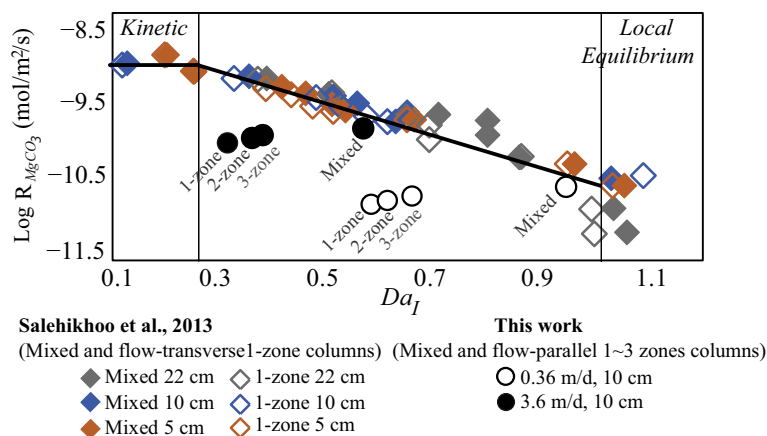


Fig. 9. $\log R_{\text{MgCO}_3}$ (mol/m²/s) (BET-surface-area-normalized rates) as a function of Da_I values, plotted for data from our previous study for Mixed and flow-transverse 1-zone columns under different flow conditions for columns of different length (5, 10, and 22 cm) (diamonds) (Salehikhoo et al., 2013), and for data from this study with Mixed and flow-parallel columns (open and filled circles). Note that although plots of $\log R_{\text{MgCO}_3}$ vs. Da_I for the Mixed columns still fall on the black line dictated by the previously derived $\log R_{\text{MgCO}_3} \sim Da_I$ relationship ($\log R_{\text{MgCO}_3} = -1.9Da_I - 8.6$, Eq. (18)), those for Three-zone, Two-zone, and One-zone columns do not. Apparently, this developed relationship does not work for systems with mineral spatial zonation patterns that limit dissolution rates.

The characteristic time scale for advection is the residence time of fluid in the column, defined as $\tau_{\text{adv}} = \frac{L}{v}$, where L is the length of the column (m) and v is the average flow velocity (m/d). The characteristic time scale for dissolution is essentially the time to reach equilibrium in the entire column. This is defined as $\tau_r = \frac{V_p C_{\text{eq,Mg}}}{R_{\text{MgCO}_3} A_T}$, where V_p is the total pore volume of the column (m³), $C_{\text{eq,Mg}}$ is the equilibrium concentration of Mg(II) (mol/m³), R_{MgCO_3} is the column-scale BET-surface-area-normalized dissolution rate (mol/m²/s), and A_T is the total BET magnesite surface area in the column (m²). The Damkohler number essentially compares the relative dominance of reaction and advection at the column scale.

Based on magnesite dissolution data in our previous work and also shown here in Fig. 9, we observe three regimes. Where advection is fast compared to dissolution (small Da_I), we observe the kinetic regime where dissolution is limiting. The rates in the kinetic regime only depend on kinetics and not on the rate of advection or the value of Da_I . In the middle regime with intermediate Da_I values, the advection and dissolution rates are comparable and depend on Da_I through the following equation shown as the black line in Fig. 9:

$$\log R_{\text{MgCO}_3} = -1.9Da_I - 8.6 \quad (18)$$

This equation was obtained by regression in our previous work, yielding a coefficient of determination (R^2) equal to 0.895. In the local equilibrium regime (large Da_I), advection is limiting and the system eventually reaches equilibrium. For the Mixed and the flow-transverse One-zone columns in our previous work, rates were limited by up to 14% in the flow-transverse columns compared to the homogeneous Mixed column. This maximal rate suppression was observed in the middle regime with intermediate Da_I values.

To understand if the column-scale rates from the flow-parallel One-zone columns in this work also follows Eq. (18), the rates were plotted on the same figure using open

and filled black circles. As expected, the rates from the Mixed column follow the black line dictated by Eq. (18). However, the rates from the flow-parallel zonation columns deviate from the regression line predicted by the equation derived for the flow-transverse zonation columns. The rates of the One-zone column deviate most from the regression line. This indicates that the ratio of the time scales of advection and reaction – i.e., the Da_I – is not sufficient to describe the rates for the flow-parallel heterogeneous columns. Some other measure must be used to characterize the corresponding rates in the zonation columns reported here.

5. CONCLUSIONS

This work compares dissolution rates in columns with magnesite packed in distinct zones to those with uniform spatial distribution. We show that mineral spatial distribution at the column scale affect their dissolution rates, which for the first time experimentally confirms conclusions from modeling studies that randomly distributed minerals with small clusters typically have higher dissolution rates than zoned distributions (Li et al., 2006, 2007a,b). We have now explored zonation that is transverse to the flow path (Salehikhoo et al., 2013) and parallel to flow path (this work). Rates from flow-parallel One-zone columns are lower than those from Mixed columns by a factor of 1.5–2, whereas rates from transverse columns are lower by only up to a factor of 1.14. This is largely because the reaction products were easily transported out of the horizontal layers of reactive minerals by advective flow in the flow-transverse case. In the flow-parallel cases in this study, the local dissolution rates are limited by the rates of mass transport out of the magnesite zone and pore fluids easily reach local equilibrium inside the reactive mineral zones. The transverse dispersivity, a measure of the mass transport rate at the magnesite–quartz interface, determines the amount of effectively dissolving magnesite grains and ultimately the

column-scale bulk dissolution rates. This observation echoes other studies that focus on bimolecular reactions occurring at the mixing “interface” of waters containing different reactants (De Simoni et al., 2007; Chiogna et al., 2011).

Importantly, our analysis based on 2D reactive transport modeling shows that the column-scale dissolution rates are not a function of total magnesite surface area. Instead, the rates strongly depend on the effective surface area A_e defined as the surface area of magnesite grains bathed in fluids that are far from equilibrium (with $IAP/K_{eq} < 0.1$). This effective surface area is a function of both flow rate and the pattern of spatial zonation. With an order of magnitude variation in flow velocity, the A_e value for these columns can vary by almost 1.5 orders of magnitude, resulting in 1.5 orders of magnitude variation in column-scale bulk dissolution rate. In our flow-parallel One-zone column experiment, only about 2% of the magnesite BET surface area was dissolving under far from equilibrium conditions at the lower flow rate of 0.36 m/d. In contrast, 67% of the BET surface area was dissolving in the Mixed column at the higher flow rate of 3.6 m/d. The column-scale bulk rates ($R_{MgCO_3,B}$, mol/s) depend on the effective surface area in the form of $R_{MgCO_3,B}$ (mol/s) = $10^{-9.56} A_e$.

This has very interesting implications for interpreting laboratory-field rate discrepancies. Extrapolating our observations, we infer that lab-field rate discrepancies may often be caused by slow flow or zonation of reactive minerals that leave some surface area bathed by equilibrated fluid and some bathed by far-from-equilibrium fluid. If we know exactly the amount of effective surface area of reactive minerals that participate in the reactions, we can approximately use the rate constant obtained in well-mixed laboratory systems. This argument on the importance of effective surface area echoes some of the discussion in literature that we should use geometric surface area, instead of total BET surface area, to calculate rates in natural systems (Gautier et al., 2001; Jeschke and Dreybrodt, 2002). Interestingly, geometric surface area is typically lower than the BET surface area. This is also consistent with some of the insights gained in modeling weathering rates in the long term that the values of surface area used has to be orders of magnitude lower than the measured BET surface area in order to match weathering data (Moore et al., 2012).

For the One-zone columns, the magnesite grains at the magnesite–quartz interface (A_i) contribute 55–73% of the overall effective surface area across all flow and spatial zonation conditions we studied here. The rest of the effective surface area (bathed in non-equilibrated porefluids) lies near the column inlet. Considering that here we have relatively short columns (10 cm) where grid blocks close to the inlet can contribute significantly to the overall rate, we expect that the interfaces of reactive mineral clusters will be more important in natural systems with longer flow paths where boundary or inlet effect is smaller. As such, a first-order estimate of the column-scale rate can be attained by using the surface area of magnesite at the interface instead of the total magnesite surface area. Importantly, the interface surface area can be determined through observation.

It is worth noting that the length scales of mineral zonation must be taken into account when scaling mineral reactions from the laboratory to the field. Consider, for example, soils that have flow-parallel mineral zones that contain either 90% reactant with 10% inert mineral surrounded by zones of 10% reactant with 90% inert material. We might successfully predict pore fluid chemistry due to mineral reaction along the flow path if our system of study was small enough that it only included the mineral-rich zone itself. In contrast, if our system of study included both the mineral-rich and mineral-poor zones, scaling from the laboratory to the field system would “discover” a rate discrepancy due to the zonation. This example points to the importance of the length scales of reactive mineral distribution in scaling reaction rates from one system to another. Scaling that crosses the characteristic length of layer spacing will show a larger laboratory-field discrepancy than scaling that does not cross this characteristic length.

While the rate discrepancies discussed here and in our previous paper may appear to be relatively small (1.14 for flow-transverse or 1.5–2 times for flow-parallel), such discrepancies result in very large differences in mineral compositions in soils or aquifers when rates have been operative over geologic time. For example, for moderately fast-eroding, relatively thin soils that are not weathering in either the kinetic or the local equilibrium regimes (Lebedeva et al., 2007, 2010), different distributions of the reacting mineral may result in soils that are very different in mineral composition. Assuming that the effects of spatial zonation for a mineral such as apatite are the same as the magnesite studied here, the soil could become depleted at different extent. Since apatite is often the ultimate source of phosphorus for plants and the depletion is generally most severe in the topsoil, such “small” rate variations can have profound implications on ecosystem function (Christophe et al., 2013). Furthermore, if the solute released during mineral dissolution is a key nutrient that sustains bacterial or plant growth, differences in spatial distribution of porefluid chemistry can largely control the patterns of biota, creating biogeochemical “hot spots”. In fact, hot spots have generally been observed at the interface of distinct zones with drastically different conditions (McClain et al., 2003). In a broader context, this indicates that mineral spatial heterogeneity can potentially dictate patterns of both biogeochemistry and ecosystem functioning.

ACKNOWLEDGEMENTS

This work is supported by the Penn State Institutes of Energy and the Environment (PSIEE) for LL. The Penn State Laboratory for Isotopes and Minerals in the Environment, and the Penn State Earth and Environmental Systems Institute provided valuable support for sample analysis. SLB cites support from DOE Office of Basic Energy Sciences DE FG02 05ER15675. We thank the associate editor Daniel E. Giammar and three anonymous reviewers for their insightful and constructive comments that have significantly improved the paper.

REFERENCES

- Alekseyev V. A., Medvedeva L. S., Prisyagina N. I., Meshalkin S. S. and Balabin A. I. (1997) Change in the dissolution rates of

- alkali feldspars as a result of secondary mineral precipitation and approach to equilibrium. *Geochim. Cosmochim. Acta* **61**, 1125–1142.
- Anbeek C. (1993) The effect of natural weathering on dissolution rates. *Geochim. Cosmochim. Acta* **57**, 4963–4975.
- Anderson S. P., Dietrich W. E. and Brimhall G. H. (2002) Weathering profiles, mass-balance analysis, and rates of solute loss: linkages between weathering and erosion in a small, steep catchment. *Geol. Soc. Am. Bull.* **114**, 1143–1158.
- Banwart S., Bernasconi S. M., Bloem J., Blum W., Brandao M., Brantley S., Chabaux F., Duffy C., Kram P., Lair G., Lundin L., Nikolaidis N., Novak M., Panagos P., Ragnarsdottir K. V., Reynolds B., Rousseva S., de Ruiter P., van Gaans P., van Riemsdijk W., White T. and Zhang B. (2011) Soil processes and functions in critical zone observatories: hypotheses and experimental design. *Vadose Zone J.* **10**, 974–987.
- Benezeth P., Saldi G. D., Dandurand J.-L. and Schott J. (2011) Experimental determination of the solubility product of magnesite at 50 to 200 degrees C. *Chem. Geol.* **286**, 21–31.
- Berkowitz B. and Scher H. (2001) The role of probabilistic approaches to transport theory in heterogeneous media. *Transp. Porous Media* **42**, 241–263.
- Bernabe Y. and Bruderer C. (1998) Effect of the variance of pore size distribution on the transport properties of heterogeneous networks. *J. Geophys. Res. Solid Earth* **103**, 513–525.
- Bernabe Y., Mok U. and Evans B. (2003) Permeability–porosity relationships in rocks subjected to various evolution processes. *Pure Appl. Geophys.* **160**, 937–960.
- Bernabe Y., Zamora M., Li M., Maineult A. and Tang Y. B. (2011) Pore connectivity, permeability, and electrical formation factor: a new model and comparison to experimental data. *J. Geophys. Res. Solid Earth* **116**.
- Biswas A., Majumder S., Neidhardt H., Halder D., Bhowmick S., Mukherjee-Goswami A., Kundu A., Saha D., Berner Z. and Chatterjee D. (2011) Groundwater chemistry and redox processes: depth dependent arsenic release mechanism. *Appl. Geochem.* **26**, 516–525.
- Brantley S. L. (2004) Reaction kinetics of primary rock-forming minerals under ambient conditions. In *Treatise on Geochemistry: Surface and Ground Water, Weathering, and Soils* (ed. J. I. Drever). Elsevier Pergamon, Amsterdam, pp. 73–118.
- Brantley S. L. (2010) Weathering: rock to regolith. *Nat. Geosci.* **3**, 305–306.
- Brantley S. L. and White A. F. (2009) Approaches to modeling weathered regolith. *Rev. Mineral. Geochem.* **70**, 435–484.
- Brusseau M. L., Nelson N. T., Oostrom M., Zhang Z. H., Johnson G. R. and Wietsma T. W. (2000) Influence of heterogeneity and sampling method on aqueous concentrations associated with NAPL dissolution. *Environ. Sci. Technol.* **34**, 3657–3664.
- Casey W. H. (1987) Heterogeneous kinetics and diffusion boundary-layers – the example of reaction in a fracture. *J. Geophys. Res. B Solid Earth Planets* **92**, 8007–8013.
- Casey W. H., Banfield J. F., Westrich H. R. and McLaughlin L. (1993) What do dissolution experiments tell us about natural weathering? *Chem. Geol.* **105**, 1–15.
- Castro-Alcala E., Fernandez-Garcia D., Carrera J. and Bolster D. (2012) Visualization of mixing processes in a heterogeneous sand box aquifer. *Environ. Sci. Technol.* **46**, 3228–3235.
- Chang H.-S., Um W., Rod K., Serne R. J., Thompson A., Perdrial N., Steefel C. I. and Chorover J. (2011) Strontium and cesium release mechanisms during unsaturated flow through waste-weathered Hanford sediments. *Environ. Sci. Technol.* **45**, 8313–8320.
- Chiogna G., Cirpka O. A., Grathwohl P. and Rolle M. (2011) Transverse mixing of conservative and reactive tracers in porous media: quantification through the concepts of flux-related and critical dilution indices. *Water Resour. Res.* **47**.
- Chorover J., Troch P. A., Rasmussen C., Brooks P. D., Pelletier J. D., Breshears D. D., Huxman T. E., Kurc S. A., Lohse K. A., McIntosh J. C., Meixner T., Schaap M. G., Litvak M. E., Perdrial J., Harpold A. and Durcik M. (2011) How water, carbon, and energy drive critical zone evolution: the Jemez-Santa Catalina critical zone observatory. *Vadose Zone J.* **10**, 884–899.
- Chou L., Garrels R. M. and Wollast R. (1989) Comparative study of the kinetics and mechanisms of dissolution of carbonate minerals. *Chem. Geol.* **78**, 269–282.
- Christophe C., Marie-Pierre T., Pascale F.-K., Stephane U., Marie-Claire P., Zornitza T. and Antoine K. (2013) Increase of apatite dissolution rate by Scots pine roots associated or not with *Burkholderia glathei* PML1(12)Rp in open-system flow microcosms. *Geochim. Cosmochim. Acta* **106**, 287–306.
- Colon C. F. J., Oelkers E. H. and Schott J. (2004) Experimental investigation of the effect of dissolution on sandstone permeability, porosity, and reactive surface area. *Geochim. Cosmochim. Acta* **68**, 805–817.
- De Simoni M., Sanchez-Vila X., Carrera J. and Saaltink M. W. (2007) A mixing ratios-based formulation for multicomponent reactive transport. *Water Resour. Res.* **43**.
- Detwiler R. L. (2010) Permeability alteration due to mineral dissolution in partially saturated fractures. *J. Geophys. Res. Solid Earth* **115**.
- Detwiler R. L., Glass R. J. and Bourcier W. L. (2003) Experimental observations of fracture dissolution: the role of Peclet number on evolving aperture variability. *Geophys. Res. Lett.* **30**.
- DiFilippo E. L., Carroll K. C. and Brusseau M. L. (2010) Impact of organic-liquid distribution and flow-field heterogeneity on reductions in mass flux. *J. Contam. Hydrol.* **115**, 14–25.
- Domenico P. A. and Schwartz F. W. (1990) *Physical and Chemical Hydrogeology*. John Wiley & Sons, New York.
- Druhan J. L., Steefel C. I., Molins S., Williams K. H., Conrad M. E. and DePaolo D. J. (2012) Timing the onset of sulfate reduction over multiple subsurface acetate amendments by measurement and modeling of sulfur isotope fractionation. *Environ. Sci. Technol.* **46**, 8895–8902.
- Frye E., Bao C., Li L. and Blumsack S. (2012) Environmental controls of cadmium desorption during CO₂ leakage. *Environ. Sci. Technol.* **46**, 4388–4395.
- Gautier J.-M., Oelkers E. H. and Schott J. (2001) Are quartz dissolution rates proportional to B.E.T. surface areas? *Geochim. Cosmochim. Acta* **65**, 1059–1070.
- Gelhar L. W. (1993) *Stochastic Subsurface Hydrology*. Prentice-Hall, Englewood Cliffs, NJ.
- Gelhar L. W. and Axness C. L. (1983) Three-dimensional stochastic analysis of macrodispersion in aquifers. *Water Resour. Res.* **19**, 161–180.
- Gelhar L. W., Welty C. and Rehfeldt K. R. (1992) A critical-review of data on field-scale dispersion in aquifers. *Water Resour. Res.* **28**, 1955–1974.
- Godderis Y., Brantley S. L., Francois L. M., Schott J., Pollard D., Deque M. and Dury M. (2013) Rates of consumption of atmospheric CO₂ through the weathering of loess during the next 100 yr of climate change. *Biogeosciences* **10**, 135–148.
- Godderis Y., Williams J. Z., Schott J., Pollard D. and Brantley S. L. (2010) Time evolution of the mineralogical composition of Mississippi Valley loess over the last 10 kyr: climate and geochemical modeling. *Geochim. Cosmochim. Acta* **74**, 6357–6374.
- Gouze P., Noiriél C., Bruderer C., Loggia D. and Leprovost R. (2003) X-ray tomography characterization of fracture surfaces during dissolution. *Geophys. Res. Lett.* **30**.

- Hamzaoui-Azaza F., Ketata M., Bouhlila R., Gueddari M. and Riberio L. (2011) Hydrogeochemical characteristics and assessment of drinking water quality in Zeuss–Koutine aquifer, southeastern Tunisia. *Environ. Monit. Assess.* **174**, 283–298.
- Hausrath E. M., Navarre-Sitchler A. K., Sak P. B., Steefel C. I. and Brantley S. L. (2008) Basalt weathering rates on Earth and the duration of liquid water on the plains of Gusev Crater, Mars. *Geology* **36**, 67–70.
- Hochstetler D. L., Rolle M., Chiogna G., Haberer C. M., Grathwohl P. and Kitanidis P. K. (2013) Effects of compound-specific transverse mixing on steady-state reactive plumes: insights from pore-scale simulations and Darcy-scale experiments. *Adv. Water Resour.* **54**, 1–10.
- Hunt A. G., Skinner T. E., Ewing R. P. and Ghanbarian-Alavijeh B. (2011) Dispersion of solutes in porous media. *Eur. Phys. J. B* **80**, 411–432.
- Iwakun O., Ulrich A., Biggar K. and Sego D. (2012) Groundwater geochemical characterization of a fuel-contaminated fractured bedrock in a permafrost environment. *J. Environ. Eng.* **138**, 958–971.
- Jeschke A. A. and Dreybrodt W. (2002) Pitfalls in the determination of empirical dissolution rate equations of minerals from experimental data and a way out: an iterative procedure to find valid rate equations, applied to Ca-carbonates and -sulphates. *Chem. Geol.* **192**, 183–194.
- Jin L., Ravella R., Ketchum B., Bierman P. R., Heaney P., White T. and Brantley S. L. (2010) Mineral weathering and elemental transport during hillslope evolution at the Susquehanna/Shale Hills Critical zone observatory. *Geochim. Cosmochim. Acta* **74**, 3669–3691.
- Johnson J. W., Oelkers E. H. and Helgeson H. C. (1992) {SUPCRT92}: a software package for calculating the standard molal thermodynamic properties of minerals, gases, aqueous species, and reactions from 1 to 5000 bar and 0 to 1000 deg {C}. *Comput. Geosci.* **18**, 899–947.
- Knapp R. B. (1989) Spatial and temporal scales of local equilibrium in dynamic fluid–rock systems. *Geochim. Cosmochim. Acta* **53**, 1955–1964.
- Krumins V., Gehlen M., Arndt S., Van Cappellen P. and Regnier P. (2013) Dissolved inorganic carbon and alkalinity fluxes from coastal marine sediments: model estimates for different shelf environments and sensitivity to global change. *Biogeosciences* **10**, 371–398.
- Landrot G., Ajo-Franklin J. B., Yang L., Cabrini S. and Steefel C. I. (2012) Measurement of accessible reactive surface area in a sandstone, with application to CO₂ mineralization. *Chem. Geol.* **318**, 113–125.
- Laverman A. M., Meile C., Van Cappellen P. and Wieringa E. B. A. (2007) Vertical distribution of denitrification in an estuarine sediment: integrating sediment flowthrough reactor experiments and microprofiling via reactive transport modeling. *Appl. Environ. Microbiol.* **73**, 40–47.
- Lebedeva M. I., Fletcher R. C., Balashov V. N. and Brantley S. L. (2007) A reactive diffusion model describing transformation of bedrock to saprolite. *Chem. Geol.* **244**, 624–645.
- Lebedeva M. I., Fletcher R. C. and Brantley S. L. (2010) A mathematical model for steady-state regolith production at constant erosion rate. *Earth Surf. Proc. Land.* **35**, 508–524.
- Li L., Gawande N., Kowalsky M. B., Steefel C. I. and Hubbard S. S. (2011) Physicochemical heterogeneity controls on uranium bioreduction rates at the field scale. *Environ. Sci. Technol.* **45**, 9959–9966.
- Li L., Peters C. A. and Celia M. A. (2006) Upscaling geochemical reaction rates using pore-scale network modeling. *Adv. Water Resour.* **29**, 1351–1370.
- Li L., Peters C. A. and Celia M. A. (2007a) Applicability of averaged concentrations in determining geochemical reaction rates in heterogeneous porous media. *Am. J. Sci.* **307**, 1146–1166.
- Li L., Peters C. A. and Celia M. A. (2007b) Effects of mineral spatial distribution on reaction rates in porous media. *Water Resour. Res.* **43**. <http://dx.doi.org/10.1029/2005WR004848>.
- Li L., Steefel C. I., Kowalsky M. B., Englert A. and Hubbard S. S. (2010) Effects of physical and geochemical heterogeneities on mineral transformation and biomass accumulation during a biostimulation experiment at Rifle, Colorado. *J. Contam. Hydrol.* **112**, 45–63.
- Lichtner P. C. (1985) Continuum model for simultaneous chemical-reactions and mass-transport in hydrothermal systems. *Geochim. Cosmochim. Acta* **49**, 779–800.
- Lichtner P. C. (1996) Continuum formulation of multicomponent-multiphase reactive transport. In *Reactive Transport in Porous Media* (eds. P. C. Lichtner, C. I. Steefel and E. H. Oelkers). Mineralogical Society of America, Washington, DC, pp. 1–81.
- Lin H., Hopmans J. W. and Richter D. d. (2011) Interdisciplinary sciences in a global network of critical zone observatories. *Vadose Zone J.* **10**, 781–785.
- Liu C., Zachara J. M., Qafoku N. P. and Wang Z. (2008) Scale-dependent desorption of uranium from contaminated subsurface sediments. *Water Resour. Res.* **44**.
- Liu C., Zachara J. M., Qafoku O., McKinley J. P., Heald S. M. and Wang Z. (2004) Dissolution of uranyl microprecipitates in subsurface sediments at Hanford Site, USA. *Geochim. Cosmochim. Acta* **68**, 4519–4537.
- Liu C. X., Shang J. Y., Kerisit S., Zachara J. M. and Zhu W. H. (2013) Scale-dependent rates of uranyl surface complexation reaction in sediments. *Geochim. Cosmochim. Acta* **105**, 326–341.
- Maher K. (2010) The dependence of chemical weathering rates on fluid residence time. *Earth Planet. Sci. Lett.* **294**, 101–110.
- Maher K. (2011) The role of fluid residence time and topographic scales in determining chemical fluxes from landscapes. *Earth Planet. Sci. Lett.* **312**, 48–58.
- Maher K., DePaolo D. J. and Lin J. C. F. (2004) Rates of silicate dissolution in deep-sea sediment: in situ measurement using U-234/U-238 of pore fluids. *Geochim. Cosmochim. Acta* **68**, 4629–4648.
- Maher K., Steefel C. I., DePaolo D. J. and Viani B. E. (2006) The mineral dissolution rate conundrum: insights from reactive transport modeling of U isotopes and pore fluid chemistry in marine sediments. *Geochim. Cosmochim. Acta* **70**, 337–363.
- McClain M. E., Boyer E. W., Dent C. L., Gergel S. E., Grimm N. B., Groffman P. M., Hart S. C., Harvey J. W., Johnston C. A., Mayorga E., McDowell W. H. and Pinay G. (2003) Biogeochemical hot spots and hot moments at the interface of terrestrial and aquatic ecosystems. *Ecosystems* **6**, 301–312.
- McGuire T. P., Elsworth D. and Karcz Z. (2013) Experimental measurements of stress and chemical controls on the evolution of fracture permeability. *Transp. Porous Media* **98**, 15–34.
- Minyard M. L. and Burgos W. D. (2007) Hydrologic flow controls on biologic iron(III) reduction in natural sediments. *Environ. Sci. Technol.* **41**, 1218–1224.
- Molins S., Trebotich D., Steefel C. I. and Shen C. (2012) An investigation of the effect of pore scale flow on average geochemical reaction rates using direct numerical simulation. *Water Resour. Res.* **48**.
- Moore J., Lichtner P. C., White A. F. and Brantley S. L. (2012) Using a reactive transport model to elucidate differences between laboratory and field dissolution rates in regolith. *Geochim. Cosmochim. Acta* **93**, 235–261.

- Morse J. W. and Arvidson R. S. (2002) The dissolution kinetics of major sedimentary carbonate minerals. *Earth-Sci. Rev.* **58**, 51–84.
- Morse J. W., Arvidson R. S. and Luttge A. (2007) Calcium carbonate formation and dissolution. *Chem. Rev.* **107**, 342–381.
- Navarre-Sitchler A. and Brantley S. (2007) Basalt weathering across scales. *Earth Planet. Sci. Lett.* **261**, 321–334.
- Newell C. J., Hopkins L. P. and Bedient P. B. (1990) A hydrogeologic database for groundwater modeling. *Ground Water* **28**, 703–714.
- Noiriel C., Renard F., Doan M. L. and Gratier J. P. (2010) Intense fracturing and fracture sealing induced by mineral growth in porous rocks. *Chem. Geol.* **269**, 197–209.
- Peng S., Hu Q., Ewing R. P., Liu C. and Zachara J. M. (2012) Quantitative 3-D elemental mapping by LA-ICP-MS of a basaltic clast from the Hanford 300 area, Washington, USA. *Environ. Sci. Technol.* **46**, 2025–2032.
- Plummer L. N. and Wigley T. M. L. (1976) The dissolution of calcite in CO₂-saturated solutions at 25 °C and 1 atmosphere total pressure. *Geochim. Cosmochim. Acta* **40**, 191–202.
- Pokrovsky O. S., Golubev S. V., Schott J. and Castillo A. (2009) Calcite, dolomite and magnesite dissolution kinetics in aqueous solutions at acid to circumneutral pH, 25 to 150 degrees C and 1 to 55 atm pCO₂: new constraints on CO₂ sequestration in sedimentary basins. *Chem. Geol.* **265**, 20–32.
- Pruess K. (2008) On production behavior of enhanced geothermal systems with CO₂ as working fluid. *Energy Convers. Manage.* **49**, 1446–1454.
- Rolle M., Eberhardt C., Chiogna G., Cirpka O. A. and Grathwohl P. (2009) Enhancement of dilution and transverse reactive mixing in porous media: experiments and model-based interpretation. *J. Contam. Hydrol.* **110**, 130–142.
- Roy S. and Tarafdar S. (1997) Archie's law from a fractal model for porous rocks. *Phys. Rev. B* **55**, 8038–8041.
- Saldi G. D., Jordan G., Schott J. and Oelkers E. H. (2009) Magnesite growth rates as a function of temperature and saturation state. *Geochim. Cosmochim. Acta* **73**, 5646–5657.
- Saldi G. D., Schott J., Pokrovsky O. S., Gautier Q. and Oelkers E. H. (2012) An experimental study of magnesite precipitation rates at neutral to alkaline conditions and 100–200 degrees C as a function of pH, aqueous solution composition and chemical affinity. *Geochim. Cosmochim. Acta* **83**, 93–109.
- Saldi G. D., Schott J., Pokrovsky O. S. and Oelkers E. H. (2010) An experimental study of magnesite dissolution rates at neutral to alkaline conditions and 150 and 200 degrees C as a function of pH, total dissolved carbonate concentration, and chemical affinity. *Geochim. Cosmochim. Acta* **74**, 6344–6356.
- Salehikhoo F., Li L. and Brantley S. L. (2013) Magnesite dissolution rates at different spatial scales: the role of mineral spatial distribution and flow velocity. *Geochim. Cosmochim. Acta* **108**, 91–106.
- Scheibe T. D., Fang Y., Murray C. J., Roden E. E., Chen J., Chien Y.-J., Brooks S. C. and Hubbard S. S. (2006) Transport and biogeochemical reaction of metals in a physically and chemically heterogeneous aquifer. *Geosphere* **2**. <http://dx.doi.org/10.1130/GES00029.00021>.
- Singha K., Li L., Day-Lewis F. D. and Regberg A. B. (2011) Quantifying solute transport processes: are chemically “conservative” tracers electrically conservative? *Geophysics* **76**, F53–F63.
- Steeff C. I., DePaolo D. J. and Lichtner P. C. (2005) Reactive transport modeling: an essential tool and a new research approach for the Earth Sciences. *Earth Planet. Sci. Lett.* **240**, 539–558.
- Steeff C. I. and Lasaga A. C. (1994) A coupled model for transport of multiple chemical species and kinetic precipitation/dissolution reactions with application to reactive flow in single phase hydrothermal systems. *Am. J. Sci.* **294**, 529–592.
- Sudicky E. A., Illman W. A., Goltz I. K., Adams J. J. and McLaren R. G. (2010) Heterogeneity in hydraulic conductivity and its role on the macroscale transport of a solute plume: from measurements to a practical application of stochastic flow and transport theory. *Water Resour. Res.* **46**.
- Taron J. and Elsworth D. (2009) Thermal–hydrologic–mechanical–chemical processes in the evolution of engineered geothermal reservoirs. *Int. J. Rock Mech. Min. Sci.* **46**, 855–864.
- Tartakovsky A. M., Redden G., Lichtner P. C., Scheibe T. D. and Meakin P. (2008) Mixing-induced precipitation: experimental study and multiscale numerical analysis. *Water Resour. Res.* **44**.
- Taylor A. S., Blum J. D. and Lasaga A. C. (2000) The dependence of labradorite dissolution and Sr isotope release rates on solution saturation state. *Geochim. Cosmochim. Acta* **64**, 2389–2400.
- Taylor K. G. and Macquaker J. H. S. (2011) Iron minerals in marine sediments record chemical environments. *Elements* **7**, 113–118.
- Van Cappellen P. and Gaillard J. (1996) Biogeochemical dynamics in aquatic sediments. In *Reactive Transport in Porous Media* (eds. P. C. Lichtner, C. I. Steeff and E. H. Oelkers). Mineralogical Society of America, Washington, DC.
- Van Grinsven J. J. M. and Van Riemsdijk W. H. (1992) Evaluation of batch and column techniques to measure weathering rates in soils. *Geoderma* **52**, 41–58.
- Velbel M. A. (1993) Constancy of silicate–mineral weathering-rate ratios between natural and experimental weathering: implications for hydrologic control of differences in absolute rates. *Chem. Geol.* **105**, 89–99.
- White A. F. (2002) Determining mineral weathering rates based on solid and solute weathering gradients and velocities: application to biotite weathering in saprolites. *Chem. Geol.* **190**, 69–89.
- White A. F. and Brantley S. L. (1995) Chemical weathering rates of silicate minerals: an overview. In *Chemical Weathering Rates of Silicate Minerals* (eds. A. F. White and S. L. Brantley). Mineralogical Society of America, Washington, DC, pp. 1–22.
- White A. F. and Brantley S. L. (2003) The effect of time on the weathering of silicate minerals: why do weathering rates differ in the laboratory and field? *Chem. Geol.* **202**, 479–506.
- Willingham T. W., Werth C. J. and Valocchi A. J. (2008) Evaluation of the effects of porous media structure on mixing-controlled reactions using pore-scale modeling and micromodel experiments. *Environ. Sci. Technol.* **42**, 3185–3193.
- Wolery T. J., Jackson K. J., Bourcier W. L., Bruton C. J., Viani B. E., Knauss K. G. and Delany J. M. (1990) Current status of the EQ3/6 software package for geochemical modeling. *ACS Symp. Ser.* **416**, 104–116.
- Yabusaki S. B., Fang Y., Williams K. H., Murray C. J., Ward A. L., Dayvault R. D., Waichler S. R., Newcomer D. R., Spane F. A. and Long P. E. (2011) Variably saturated flow and multicomponent biogeochemical reactive transport modeling of a uranium bioremediation field experiment. *J. Contam. Hydrol.* **126**, 271–290.
- Yoon H., Oostrom M., Wietsma T. W., Werth C. J. and Valocchi A. J. (2009) Numerical and experimental investigation of DNAPL removal mechanisms in a layered porous medium by means of soil vapor extraction. *J. Contam. Hydrol.* **109**, 1–13.
- Yoon H., Valocchi A. J., Werth C. J. and Dewers T. (2012) Pore-scale simulation of mixing-induced calcium carbonate precipitation and dissolution in a microfluidic pore network. *Water Resour. Res.* **48**.
- Yoon H., Werth C. J., Valocchi A. J. and Oostrom M. (2008) Impact of nonaqueous phase liquid (NAPL) source zone architecture on mass removal mechanisms in strongly layered

- heterogeneous porous media during soil vapor extraction. *J. Contam. Hydrol.* **100**, 58–71.
- Zhang C., Dehoff K., Hess N., Oostrom M., Wietsma T. W., Valocchi A. J., Fouke B. W. and Werth C. J. (2010) Pore-scale study of transverse mixing induced CaCO_3 precipitation and permeability reduction in a model subsurface sedimentary system. *Environ. Sci. Technol.* **44**, 7833–7838.
- Zhang C. Y., Yoon H., Werth C. J., Valocchi A. J., Basu N. B. and Jawitz J. W. (2008) Evaluation of simplified mass transfer models to simulate the impacts of source zone architecture on nonaqueous phase liquid dissolution in heterogeneous porous media. *J. Contam. Hydrol.* **102**, 49–60.
- Zhu C. (2005) In situ feldspar dissolution rates in an aquifer. *Geochim. Cosmochim. Acta* **69**, 1435–1453.
- Zhu C., Lu P., Zheng Z. and Ganor J. (2010) Coupled alkali feldspar dissolution and secondary mineral precipitation in batch systems: 4. Numerical modeling of kinetic reaction paths. *Geochim. Cosmochim. Acta* **74**, 3963–3983.
- Zhu C. and Schwartz F. W. (2011) Hydrogeochemical processes and controls on water quality and water management. *Elements* **7**, 169–174.

Associate editor: Daniel E. Giammar